Inhibitory control of locomotor statistics in walking *Drosophila*

Hannah Gattuso[1], Kavin Nuñez[1], Beatriz de la Rea[1], Bard Ermentrout[2], Jonathan Victor[3], Katherine Nagel[1*]

[1] Department of Neuroscience, NYU School of Medicine, 435 E 30th St. New York, NY 10016, USA
[2] Department of Mathematics, University of Pittsburgh, Pittsburgh, PA, USA
[3] Feil Family Brain and Mind Research Institute, Weill Cornell Medicine, New York, NY, USA
* email: katherine.nagel@nyumc.org

Abstract

In order to forage for food, many animals regulate not only specific limb movements but the statistics of locomotor behavior over time, for example switching between long-range dispersal behaviors and more localized search depending on the availability of resources. How pre-motor circuits regulate such locomotor statistics is not clear. Here we took advantage of the robust changes in locomotor statistics evoked by attractive odors in walking *Drosophila* to investigate their neural control. We began by analyzing the statistics of ground speed and angular velocity during three well-defined motor regimes: baseline walking, upwind running during odor, and search behavior following odor offset. We find that during search behavior, flies adopt higher angular velocities and slower ground speeds, and tend to turn for longer periods of time in one direction. We further find that flies spontaneously adopt periods of different mean ground speed, and that these changes in state influence the length of odor-evoked runs. We next developed a simple physiologically-inspired computational model of locomotor control that can recapitulate these statistical features of fly locomotion. Our model suggests that contralateral inhibition plays a key role both in regulating the difference between baseline and search behavior, and in modulating the response to odor with ground speed. As the fly connectome predicts decussating inhibitory neurons in the lateral accessory lobe (LAL), a pre-motor structure, we generated genetic tools to target these neurons and test their role in behavior. Consistent with our model, we found that activation of neurons labeled in one line increased curvature. In a second line labeling distinct neurons, activation and inactivation strongly and reciprocally regulated ground speed and altered the length of the odor-evoked run. Additional targeted light activation experiments argue that these effects arise from the brain rather than from neurons in the ventral nerve cord, while sparse activation experiments argue that speed control in the second line arises from both LAL neurons and a population of neurons in the dorsal superior medial protocerebrum (SMP). Together, our work develops a biologically plausible computational architecture that captures the statistical features of fly locomotion across behavioral states and identifies potential neural substrates of these computations.

Introduction

To search for food, animals must control both the instantaneous movement of their limbs as well as statistical features of locomotion that alter their overall path through their environment and embody their search strategy. For example, seabirds decrease flying speeds and increase turning maneuvers in response to prey encounters (Paiva et al., 2010; Sommerfeld et al., 2013). Beetles and hoverflies exhibit similar strategies of area-restricted search (Banks, 1957; Chandler, 1969; Fleschner, 1950; Murdie and Hassell, 1973; Dorfman et

al., 2022). The nematode *c. elegans* shifts between wide-spread exploratory runs and localized dwelling in response to changes in the availability of food (Ben Arous et al., 2009; Shtonda and Avery, 2006). Similarly, both larval and adult *Drosophila* alter turn statistics in response to changes in odor concentration (Gomez-Marin et al. 2011, Davies et al 2015, Steck et al 2013, Alvarez-Salvado et al 2018, Demir et al. 2020, Stupski et al. 2023). How motor and premotor circuitry are organized to regulate these statistical features of locomotion is not clear.

In recent years, walking adult *Drosophila* has emerged as a powerful model for investigating the neural control of locomotion. In fruit flies, roughly 350 to 500 pairs of descending neurons (DNs) carry motor signals from the brain to the ventral nerve cord, the insect equivalent of the spinal cord (Hsu and Bhandawat, 2016, Namiki et al, 2018, Cheong et al. 2024). Individual DNs have been identified that generate forward walking, turning, or both, when activated (Cande et al. 2018, Rayshubsky et al. 2020, Bidaye et al. 2020, Yang et al. 2023). Other DNs promote stopping behavior (Cande et al. 2018, Carreira-Rosasrio et al. 2018, Lee and Doe, 2021, Sapkal et al. 2023). While a small handful of DNs appear to function as “command-like neurons” and generate specific locomotor gestures, imaging studies suggest that many more DNs participate in locomotor control (Yang et al. 2023, Aymanns et al. 2022, Bresovec et al. 2023, 2024). Further, graded activity in specific DNs or brain regions often correlates with locomotor features; in particular, bilateral activity often correlates with forward velocity while differences in activity across the two brain hemispheres correlate with angular velocity to the left or right (Bidaye et al. 2020, Rayshubsky et al. 2020, Yang et al. 2023, Bresovec et al. 2023, 2024). Finally, activation of command-like DNs in headless flies argues that interactions between DNs within the brain are crucial to generate coordinated behaviors such as walking and turning (Braun et al. 2023). Together these studies argue that locomotor features such as forward and angular velocity must be encoded by population activity across many DNs.

Complementing this experimental dissection of locomotion, many recent studies have sought to build computational models of walking behavior in flies. Several studies have used Hidden Markov Models to identify behavioral motifs during walking (Berman et al 2016, Katsov et al 2017, Tao et al 2019, Tao et al 2020, Calhoun et al 2019). These models assume that walking behavior can be parsed into discrete motifs that evolve at a set of specific timescales. In contrast, dimensionality reduction approaches suggest that fly walking evolves in a continuous state space (DeAngelis et al. 2019, York et al. 2022), while studies of odor-evoked navigation argue that walking behavior can be modulated at multiple timescales by sensory input (Alvarez-Salvado et al. 2018, Demir et al. 2020, Jayaram et al. 2023). Computational models of walking that feature biologically plausible architectures and generate continuous but low-dimensional variation in walking behavior have been lacking.

In this work, we leverage odor driven changes in locomotion to investigate and model the neural control of locomotor statistics. We find that search behavior driven by odor loss involves changes in both ground speed and angular velocity distributions, as well as an increase in unidirectional turning that alters the correlation time of angular velocity. We assess natural variation in locomotor behavior and uncover persistent periods of preferred ground speed that correlate with the intensity of the odor response. We next develop a simple but biologically plausible computational model of locomotor control by a population of DN-like units, and show that changes in inhibition in this model can recapitulate the shifts in locomotor statistics that we observe experimentally. Finally, guided by connectome data, we develop two genetic lines that target inhibitory populations in a pre-motor center known as the Lateral Accessory Lobe (LAL). We find that activation of one line increases curvature, consistent with our predictions for inhibition between hemispheres, while a second line bidirectionally controls locomotor speed and the length of odor-evoked runs. Sparse genetic analysis of the second line reveals that speed control arises at a population level from neurons in both the LAL and the dorsal superior medial protocerebrum (SMP), a region recently implicated in forward velocity control through pan-neuronal imaging (Bresovec et al. 2024). Our work highlights a simple computational architecture that can capture the statistical features of locomotion across states and identifies neural populations that can regulate the statistical features of locomotion.

Results

Locomotor statistics in walking flies vary both spontaneously and in response to sensory stimuli

In response to attractive odor, walking flies first run upwind, then often perform local search behavior following the loss of odor (Álvarez-Salvado *et al*, 2018, Demir et al. 2020). To understand how this local search behavior is generated, we began by analyzing the statistics of ground speed and angular velocity in a previously collected set of behavioral trajectories (Álvarez-Salvado *et al*, 2018, see Methods). In these experiments, flies were placed in small (14 by 4cm) wind tunnels (Fig. 1A) with laminar air flow at ~12cm/s and presented with a 10 second pulse of appetitive odor (10% apple cider vinegar) that produced an upwind run followed by local search (Fig. 1B,C). We examined the distribution of ground speeds and angular velocities in the 10 seconds following odor offset and compared these to baseline locomotion prior to odor exposure (Fig. 1D-E, Supp Fig. 1A). We found that following odor offset, flies favor lower ground speeds and larger angular velocities (Fig. 1D-E), leading to higher angular dispersion (Supp Fig. 1B). In contrast, turn frequency did not change significantly (Supp Fig. 1C). We also noticed that following odor offset, flies often turned in the same direction for extended periods of time, a behavior not seen during baseline walking (Fig. 1C, arrows). We quantified this behavior by computing the autocorrelation of angular velocity: the autocorrelation widened during offset search, compared to baseline (Fig. 1F). Thus, three statistical features of locomotion underlie the shift from baseline behavior to local search: reduced ground speed, increased angular velocity, and longer history dependence in angular velocity. Notably, search behavior is characterized by a shift in the distributions and correlations of locomotor parameters, rather than a distinct set of behavioral motifs, and the transition from search back to baseline behavior appears to be rather continuous.

We next examined spontaneous changes in locomotor behavior in trajectories without odor presentation from the same data set. Fruit flies naturally demonstrate periods of slow, local movement with many turns and periods of quick, wide-spread movement, with infrequent turns (Fig. 2A). We used a change point detection algorithm to segment spontaneous walking into epochs with different mean ground speeds (Fig 2B). The distribution of mean ground speeds revealed two peaks (Fig. 2C): a peak near zero (when flies were stopped), and a range of ground speeds from 5-20mm/s. Plotting mean angular velocity for each epoch as a function of mean ground speed revealed that angular velocity and ground speed grow linearly at low ground speeds (<5mm/s, arrow), but that mean angular velocity decreases at higher ground speeds (Fig. 2D). We additionally examined whether ground speed and angular velocity exhibit correlations on the timescale of individual turns. We used a thresholding algorithm to extract turns, and sorted the associated behavioral segments by the mean ground speed in the half second prior to the turn (Fig. 2E). We found that at high ground speeds, turns are associated with a brief drop in ground speed. This relationship is not present at low ground speeds. Thus, ground speed and angular velocity exhibit complex interactions on multiple timescales.

Finally, we asked whether the locomotor state of the fly can affect its response to a sensory stimulus. We sorted trials based on the mean ground speed of the fly prior to odor onset. Trajectories where flies were moving slowly prior to odor encounter were shorter and less dispersed (Fig. 2F). These flies reached slower peak ground speeds during the odor period and returned to slower average speeds after odor offset (Fig. 2G). In contrast, the size of the wind-orientation response was largely un-affected by behavioral state, although the orienting response was slightly delayed in flies that were moving slowly (Fig. 2H). This analysis indicates that epochs of different mean ground speed reflect states associated with different responses to a sensory stimulus. In particular, the length of the odor-evoked run appears to depend on the ground speed prior to odor encounter.

A physiologically-inspired model of locomotor control

We next sought to develop a physiologically-inspired conceptual model of locomotor control that could account for the statistics we observed experimentally— in particular the shifts in statistics that occur between baseline walking and search behavior, and the changes in odor-evoked run length with baseline ground speed state. As our starting point, we considered that (1) multiple DNs contribute to both forward and angular velocity (Rayshubskiy et al. 2020, Yang et al. 2023, Braun et al. 2023), (2) different units make different contributions to forward versus angular velocity (Rayshubskiy et al. 2020, Yang et al. 2023, Bresovec et al. 2024, Aymanns et al, 2022), (3) bilateral activity correlates with forward velocity while activity differences between hemispheres correlate with angular velocity, both in some single neurons (Bidaye et al. 2020, Yang et al. 2023), and in population imaging (Bresovec et al. 2024, Aymanns et al. 2022), and (4) distinct sets of DNs promote stopping (Lee and Doe 2021, Sapkal et al. 2023). Based on these considerations, we developed a simple model of locomotor control (Fig. 3A-D). In this model, each DN-like unit (u_1-u_5) can interact with the other units and makes a distinct contribution to overall locomotion (Fig. 3A,B). The u_3 unit promotes stopping when active. In the absence of u_3 activity, population activity across the remaining units drives locomotion. Forward velocity reflects a weighted sum of activity in the bilateral pairs u_1, u_5 and u_2, u_4, while angular velocity reflects a weighted sum of the differences in activity across these pairs. u_1 and u_5 have larger coefficients for forward velocity (α,β), while u_2 and u_4 have larger coefficients for angular velocity (γ,δ). Though highly simplified, this model captures the intuition that forward and angular velocity are regulated by graded activity across a population of DNs that can contribute differentially to these two parameters. The model coefficients (α,β,γ,δ) can be tuned to produce ground speed and angular velocity distributions similar to those observed experimentally (Supp. Fig 2A). By design, the model can reproduce the effects of activation in DNp09, in which unilateral activation produces ipsilateral turning, while bilateral activation produces an increase in ground speed (Bidaye et al. 2020, Supp Fig. 2B). The model can also reproduce the effects of activating Pair1 neurons that drive stopping (Lee and Doe 2021, Supp Fig. 2C).

We next considered how activity arises dynamically in these DN-like units (Fig. 3C). Connectomic analysis suggests that different DNs promoting turning receive input from largely non-overlapping upstream neurons (Yang et al. 2023). Therefore, each unit in our model receives an independent Gaussian noise input, ω_i. Experiments in headless flies also suggest that DNs interact directly or indirectly within the brain to generate walking and turning behavior (Braun et al. 2023). Thus, our units can interact with themselves and each other through an interaction matrix M (Fig 3C). In our model, this matrix contains only three kinds of entries: a self-excitation term for each unit (black), bidirectional inhibitory interactions between the stop unit and all others (stop inhibition, magenta), and bidirectional inhibition between locomotor units in the two hemispheres (contralateral inhibition, blue). Activity in the units is limited by a sigmoidal activation function which prevents activity from growing without bound (see Methods). We also added an interaction term between forward and angular velocities to generate sharper large turns (Fig. 3D), based on our observation of slowing before large turns at high velocity in our data (Fig. 2E), but this interaction does not impact the dynamics of the underlying unit activity.

Using this model, we asked if we could reproduce the shift between the statistics of baseline walking, and those of search behavior evoked by odor offset. With fixed parameters for self-excitation and stop inhibition, we found that increasing the magnitude of contralateral inhibition (I_c) could shift the model from relatively straight trajectories resembling baseline walking to more tortuous trajectories resembling local search (Fig. 3E). In the absence of contralateral inhibition, left and right turns are intermingled (black arrows) resulting in generally straight and dispersive trajectories. In contrast, in the presence of contralateral inhibition, trajectories feature long runs of repeated turns in the same direction (blue and cyan arrows), similar to what we

observe during search behavior evoked by odor offset. Quantitatively, increasing contralateral inhibition shifts the distribution of forward velocities to lower values, shifts the distribution of angular velocities to larger values, and widens the autocorrelation of angular velocity (Fig. 3F), similar to what we observed experimentally following odor offset. In the absence of contralateral inhibition, activity in locomotor units is correlated with each other, and anti-correlated with the stop unit, while in the presence of contralateral inhibition, units on the left and right become anti-correlated with one another (Supp. Fig. 2D), leading to larger angular velocities and lower forward velocities. Thus, a single parameter of the model governs the statistics of locomotor dispersal and smoothly switches behavior between baseline and search regimes.

We next asked if the model could reproduce the modulation of the odor response with baseline groundspeed. To generate an odor response, we incorporated two odor-gated terms into our model (Fig 3G): an odor-driven suppression of the stop unit (u_3) and a steering function that depends on the angle of the fly with respect to the upwind direction. This steering function might represent the output of PFL3 steering neurons in the central complex (Matheson et al. 2022, Westeinde et al. 2024, Mussels Pires et al. 2024), which are known to impinge on descending neurons controlling steering (Westeinde et al. 2024), and has previously been used to model upwind drive during olfactory navigation (Álvarez-Salvado et al., 2018). These two additions produce an upwind run during odor, while increasing contralateral inhibition can then produce search behavior at odor offset (Supp. Fig 2E).

To modulate baseline groundspeed, we added feed-forward inhibition that could directly control the activity of all locomotor units (Fig. 3G). As expected, increasing feed-forward inhibition encouraged slower ground speeds, while reducing feed-forward inhibition shifted the model to faster groundspeeds (Fig. 3H). We then asked how this modulation of baseline groundspeed impacted the response to an odor stimulus. Strikingly, increasing or decreasing feed-forward inhibition caused the odor-evoked run to shrink or grow, similar to what we observed experimentally during spontaneous behavioral states (Fig. 3I). Thus, the conceptual architecture we describe here, in which DN-like units receive both steering and speed control signals and jointly regulate forward and angular velocity, allows a state-dependent signal to scale the response to a sensory stimulus, as observed in our experimental data.

An advantage of this simple conceptual framework is that it is amenable to mathematical analysis, which allows us to understand its behavior. As described in the Mathematical Appendix, the dynamics of the units can be decomposed into two subsystems through a linear transformation of coordinates: a symmetric subsystem that controls forward velocity, and an anti-symmetric subsystem that controls angular velocity. The inputs to the units, such as the steering commands and feedforward inhibition, can be expressed in this new coordinate system, where it is clear that steering only impacts the anti-symmetric subsystem, while feed-forward inhibition only impacts the symmetric subsystem. This explains how these two multiplexed signals can independently control orientation and speed.

This analysis also allows us to understand why increasing contralateral inhibition shifts the model from relatively straight trajectories to more tortuous ones. The dynamics of the anti-symmetric subsystem (which controls turning) depend on its eigenvalues; when these are all negative, the model exhibits stable fixed-point dynamics, and activity returns to zero— the only stable point under these conditions — following an input. In this regime, turns to the left and right are interspersed, and the model produces mostly straight trajectories (Supp. Fig. 3, white background). In contrast, when the anti-symmetric system has a positive eigenvalue, the fixed point at zero becomes unstable and tends to go towards one of the saturation points, until noise pushes it back towards zero. Under these conditions, the model produces runs of repeated turns in the same direction, resulting in more tortuous looping trajectories (Supp. Fig. 3, gray background). The duration of these runs increases with the strength of contralateral inhibition, and depends on the amount of instability, as well as on the characteristics of the noise.

The eigenvalues of the anti-symmetric system depend on both the self-excitation parameter and on contralateral inhibition (Supp. Fig. 3). However, we find the that the model is most flexible when self-excitation is set at the transition point from stable to unstable behavior (Supp. Fig. 3, middle row). In this regime, small changes in contralateral inhibition smoothly shift the model from relatively straight to relatively tortuous trajectories. When self-excitation places the model mostly in the stable regime (top row), much larger values of contralateral inhibition are required to generate search-like trajectories, while when self-excitation places the model in the unstable regime (bottom row), trajectories are unrealistically tortuous even without contralateral inhibition. For this reason, for the simulations shown in Fig. 3, we have set the self-excitation term to this transition point. Our model and analysis suggest that a locomotor network poised between stable and unstable regimes may allow an animal to smoothly regulate the tortuosity of its trajectories through graded changes in inhibition between the two hemispheres.

Finally, we show analytically that the model exhibits similar dynamics regardless of the number of locomotion-promoting units on each side, so long as the structure of the interaction matrix M is maintained. In particular, the role of contralateral inhibition in governing the tortuosity of trajectories remains the same, regardless of the number of units. In the fly brain, multiple DN types have been identified that show activity correlated with turning (Yang et al. 2023, Aymanns et al. 2022) and the number of such units likely varies across species (Okada et al. 2003, Staudacher 1998). Thus, the analysis presented here, and the proposed role of contralateral inhibition in governing tortuosity, should apply to real biological networks with variable numbers of locomotor control units.

Inhibitory premotor neurons provide complementary control of locomotor statistics

Our model and analysis suggest that inhibition— in particular contralateral inhibition between the two hemispheres— might play a key role in shaping locomotor statistics. We therefore sought inhibitory populations that might represent correlates of the inhibition predicted by our model. The hemibrain connectome (Scheffer et al. 2020) reveals that the lateral accessory lobe (LAL), a pre-motor center strongly implicated in steering (Kanzaki et al. 1994, Namiki and Kanzaki, 2016), contains several populations of decussating neurons that are predicted to express glutamate (Eckstein et al. 2023), an inhibitory transmitter in the central fly brain (Liu and Wilson 2013). We therefore sought to gain genetic access to these populations. We identified two contralaterally projecting LAL populations, each targeted by a distinct driver line (31A11-Gal4, and VT043158-Gal4). To specify the LAL neurons labeled by each line, we used the split-Gal4 system to combine a VGlut-AD hemidriver with a DBD hemidriver for each line. The resulting split-Gal4 lines (Fig. 4A, 5A) clearly labeled contralaterally-projecting neurons in the LAL, although several additional neurons were also labeled in each line.

We next sought to investigate the effects of manipulating activity in these two lines. Activation of the first line (VGlut-AD;31A11-DBD, Fig. 4A) with Chrimson drove a decrease in ground speed and an increase in angular velocity during the activation period, resulting in an increase in curvature (Fig. 4B,C). We therefore named this line Tortuous-Gal4. Overall, the effects of activating this line were similar to increasing contralateral inhibition in our model, and to the effects of odor offset: the groundspeed distribution shifted towards lower values, the angular velocity distribution shifted slightly towards higher values, and the autocorrelation of angular velocity widened very slightly (Fig. 4D). Although the effects size is small, these results provide experimental support for the hypothesis that contralateral inhibition can alter locomotor statistics to produce search-like behavior. Silencing of this population with GtACR showed no significant effect on motor output and did not abolish odor-evoked offset search (Supp Fig. 4A,B). One possible interpretation is that these neurons form part of a larger population that contributes to search behavior during odor offset.

The Tortuous-Gal4 line also labels some neurons in the ventral nerve cord (VNC, Supp Fig 4C), which we were not able to suppress using genetic means (since tsh-GAL80 in not able to suppress split-Gal4 expression (Guo et al. 2019)). To determine whether brain or VNC neurons were responsible for the activation phenotype, we used optical fibers to target light either to the head or the VNC of a fly while measuring walking behavior on a spherical treadmill (Fig 4E). We found that targeted activation of the head drove a stronger behavioral response than equal levels of stimulation aimed at the VNC (Fig 4F). Turning behavior (absolute angular velocity) increased with increasing light level from the head fiber (Fig. 4G). These results support the idea that graded activation of head neurons in Tortuous-Gal4 can regulate turning behavior in a graded manner. We putatively identified the LAL neurons labeled by this line as LAL091-095 (Supp Fig. 4D), although it is possible that other brain neurons in this line contribute to the observed phenotype. This population receives input from PFL2 neurons that have been shown to drive slowing and increased turning (Westeinde et al. 2024) similar to the phenotype we observe with activation of Tortuous-Gal4. Neurons in this population do not synapse directly onto DNs but do make di-synaptic connections to DNs through AOTU019. These data suggest that contralateral inhibition within the brain can shape locomotor output in the manner predicted by our model, although the group of neurons we labeled are not required for the local search behavior observed at odor offset.

Optogenetic manipulation of the second line (VGlut-AD;VT043158-DBD, Fig. 5A) produced strikingly different effects on locomotor behavior. Activating this line with Chrimson strongly decreased ground speeds (Fig. 5B), while silencing this line with GtACR increased ground speeds to an atypical range (Fig. 5C). We therefore named this line Throttle-Gal4. We next asked how optogenetic manipulation of this line affects the response to an odor pulse. In interleaved trials we measured behavioral responses to an odor pulse (1% ACV) with and without optogenetic activation or silencing of Throttle-Gal4 neurons (Fig. 5D). We found that activation of Throttle-Gal4 decreased the length of upwind runs while silencing lengthened these runs (Fig. 5D,E), similar to the predictions of our model for feedforward inhibition.

To rule out the possibility that VNC neurons labeled in this line (Supp Fig. 5A) are responsible for the behavioral phenotype, we performed optical fiber experiments on a walking ball, as we had done for Tortuous-Gal4. We found that targeted light activation of the head at low intensity in Throttle-Gal4>UAS-Chrimson flies decreased forward velocity, while the same light intensity directed towards the VNC did not (Fig 5F). Likewise, low intensity targeted silencing of the head in Throttle-Gal4>UAS-GtACR flies drove an increase in forward velocity, while the same light intensity directly towards the VNC did not (Fig 5G). Light inactivation from the rear produced weaker changes in behavior than light directed from the front over all intensities surveyed (Fig. 5H). Electrophysiological recordings from LAL neurons labeled in this line revealed highly reliable tonic activity that was not strongly modulated by olfactory input (Fig. 5I,J), consistent with the idea that these neurons might encode a longer-lasting behavioral state.

In addition to the LAL, Throttle -Gal4 also labels a group of neurons in the dorsal superior medial protocerebrum (SMP) whose location and morphology are reminiscent of the Bolt PN (Bidaye et al. 2020) that promotes strong forward running. We therefore wondered whether these neurons might be responsible for the behavioral effects of activation. To address this question, we used the SPARC system (Isaacman-Beck et al. 2020) to drive sparse expression of Chrimson under control of Throttle-Gal4. We collected behavior for individual flies, then dissected and stained each brain to determine which neurons were labeled. Using both 5% and 15% expression constructs, we obtained 53 brains each with between 1-7 neurons labeled. In a few brains, we observed single neuron clones associated with behavioral phenotypes. For example, Fig. 6A shows a single LAL neuron associated with strong stopping behavior, while Fig. 6B shows a single SMP neuron associated with a much weaker slowing phenotype. Most single neuron clones were associated with relatively weak phenotypes (additional examples shown in Supp Fig. 5B).

More robust phenotypes arose from brains with multiple neurons labeled (Fig. 6C). To quantify the relationship between neural labeling and behavior, we performed a principal component analysis on the average groundspeed and angular velocity traces for each fly (Fig. 6D,E). The first principal component consisted of a drop in both forward and angular velocity specifically during the activation period, while the second principal component consisted of a slower and more long-lasting increase in both forward and angular velocity (Fig. 6D). Together these two principal components accounted for 29% of the variance across flies (Fig. 6E) and suggest that neurons in this line co-regulate forward and angular velocity (in contrast to Tortuous-Gal4, which oppositely regulates forward and angular velocity to modulate curvature). We then blindly scored neurons in each brain as belonging to dorsal SMP, dorsal LAL, medial LAL, ventral LAL, or other (see Methods), and plotted the number of neurons of each type as a function of that fly's projections onto PC1 and PC2 (Fig. 6F,G). This analysis suggests that SMP neurons contribute to the slowing phenotype in PC1 as brains with multiple SMP neurons labeled tended to have higher PC1 scores (Fig. 6F). In addition, based on principle component analysis, it is likely that medial LAL neurons contribute to slowing while dorsal and ventral LAL neurons might contribute more strongly to the speeding phenotype in PC2 (Fig. 6G, Supp Fig. 5C). Still, the heterogeneity of responses makes it difficult to assign distinct functions to each subpopulation.

We putatively identified the SMP neurons labeled in this line as SMP092, which are also predicted to be glutamatergic, and the LAL neurons as LAL 073-074 (dorsal LAL), LAL120-123 (medial LAL), and LAL124-126 (ventral LAL). These LAL neurons are highly interconnected (Supp Fig. 5D), synapsing onto their contralateral partners, as well as sending ipsilateral connections to other neurons within the population. They receive strong, bilateral input from PFL2 and PFL3, two central complex populations involved in steering and slowing when a fly is off-target (Westeinde et al. 2024, Mussells Pires et al. 2024), as well as from several atypical MBONs (Li et al, 2020), and output to multiple DNs that have been implicated in walking, including DNa02. Thus, the connectivity of these neurons is consistent with them playing a role in feed-forward inhibition, as predicted by our model. Together, these data provide experimental evidence that inhibition can shape the statistics of locomotion, likely by acting directly or indirectly on descending neurons that encode locomotor features through population activity.

Discussion

Statistical analysis of odor-evoked locomotor behavior

During foraging, many animals respond to food odor cues by altering the statistics of their locomotion to focus search behavior on one location or to disperse more widely (Shtonda and Avery 2006, Ben Arous et al 2009, Davies et al 2015, Steck et al 2013, López-Cruz et al 2019, Leitch et al. 2021). Fruit flies, in particular, have been shown to respond to the loss of an attractive odor with head casting in larvae (Gomez-Marin et al. 2011), casting behavior in flight (van Breugel et al. 2014), or local search when walking (Alvarez-Salvado et al. 2018, Demir et al. 2020). Previous studies have described this local search behavior as an increase in turn frequency (Alvarez-Salvado et al. 2018, Demir et al. 2020). Here we performed a careful statistical analysis of search behavior triggered by the loss of odor in walking flies and show that, rather than representing a change in turn frequency, local search arises from systematic shifts in the distribution and correlation of locomotor parameters.

We further explored variation in odor-evoked behavior and found that the length of the odor-evoked run depends on baseline groundspeed. We observed an effect of baseline groundspeed in spontaneous behavior and could accentuate this by experimentally manipulating groundspeed using our newly-discovered Throttle-Gal4 line. In contrast, upwind turning behavior was slightly slower in non-moving flies, but reached the same

endpoint. These results argue that speed and direction can be encoded separately to produce an upwind run during odor.

A modeling framework for population control of locomotion

Previous models of walking behavior in *Drosophila* have largely used variations of Hidden Markov Models (HMMs, Katsov et al 2017, Calhoun et al 2019, Tao et al 2019). These models rely on behavioral segmentation and classification and assume that walking can be decomposed into a series of discrete motifs. However, assessment of fruit fly walking over long periods of time suggests that behavior evolves on longer timescales that cannot be captured through a pure Markovian process (Berman et al 2016). Nested HMMs and those with dynamic transition matrices take steps towards capturing the multiple timescales of evolution within walking behavior (Calhoun et al 2019, Tao et al 2019, Demir et al 2020). Non-Markovian models of fruit fly walking, on the other hand, more accurately capture long term shifts in behavior caused by odor stimuli (Alvarez-Salvado et al 2018) but fail to accurately capture natural distributions of forward and angular velocity. While current models of fruit fly walking capture different aspects of behavioral dynamics, few provide insight into the underlying neural structures that govern locomotor statistics.

Here we developed a simple modeling framework for continuous control of locomotion by a population of DN-like units. The key aspects of this model are: (1) each unit makes a unique contribution to forward and angular velocity such that these parameters are controlled by activity across the populations a whole, and (2) units interact through a connectivity matrix that allows activity in one unit to influence the others. This modeling framework leads to several insights about the neural control of locomotion. First, we find that this simple model can generate realistic distributions of forward velocity, angular velocity, and angular velocity correlations in a variety of different behavioral states. Our model suggests that inhibition may play a key role in regulating these distributions to control tortuosity and speed, a prediction we test and confirm experimentally. In particular, we find that one form of inhibition can regulate tortuosity by altering interactions between units, while a second form of inhibition can regulate speed independent of turning by modulating all units together. Future studies with more specific driver lines may allow us to more directly test the relationship between the connectivity of inhibitory neurons and their behavioral function.

Second, we find that the model is most flexible in producing distinct locomotor patterns when its parameters position its dynamics at the edge of instability. In the stable regime, fluctuations in internal signals rapidly return to zero, so there are few sustained periods of turning in one direction or the other, even in the absence of a stabilizing external “goal” signal. In the unstable regime, fluctuations can push the unit activity towards extreme values, where they remain until rare, large noise fluctuations cause them to return to zero, resulting in prolonged turning in one direction. We find that when the model is positioned at the border between these two regimes, graded increases in inhibition can smoothly increase the propensity to instability and prolonged turning. This prediction of our model is supported by our finding that graded increases in the activity of Tortuous-Gal4 neurons result in graded increases in turning and could be further tested experimentally through population imaging of DN activity during baseline versus search states evoked by odor input (Aymanns et al. 2022, Bresovec et al. 2024).

Finally, we find analytically that the dynamics of the model do not depend on the number of units per side. This implies that similar dynamics and control principles might be found in a variety of nervous systems with different numbers of descending locomotor control neurons. In the future, we envision that our model framework could be expanded to include more realistic numbers of DNs (Namiki et al. 2018) and connectivity drawn from *Drosophila* connectomes (Scheffer et al. 2020, Cheong et al. 2024). This would allow us to compare the dynamics of real connectivity matrices to those of the idealized one investigated here.

Identification of neural populations controlling tortuosity and speed

As proof of principle that inhibition can alter locomotor statistics in the manner predicted by our model, we developed two genetic lines labeling glutamatergic neurons that alter curvature and speed respectively when activated. Targeted light experiments argue that these neural populations reside in the brain and that each population can control curvature (Tortuous-Gal4) or speed (Throttle-Gal4) in a graded manner depending on activity level. Sparse optogenetic experiments in Throttle-Gal4 argue that speed control arises from activity in both specific LAL neurons and SMP neurons, and that robust speed modulation requires co-activation of multiple neurons, arguing for a population code, similar to the population code for wingbeat amplitude recently described for fly flight (Namiki et al. 2022). However, additional experiments using more specific driver lines and/or laser activation of specific populations will be necessary to determine exactly which neurons contribute to the observed behavioral phenotypes. These caveats aside, the ability to control walking speed and curvature experimentally using these lines may aid in dissecting neural circuits for complex behaviors such as courtship (Calhoun et al. 2019) and path integration (Kim and Dickinson 2017) by allowing the investigator to acutely perturb the fly's trajectory.

In vertebrates, distinct areas of the midbrain and brainstem have been shown to regulate speed and turning behavior across species. The mesencephalic locomotor region (MLR) can initiate and control locomotor speed across terrestrial, aquatic, and avian species (Shik et al. 1966, Kashin et a.l 1974, Sirota et al. 2008, Steeves et al. 1987). Similarly, in both mice and zebrafish, a homologous set of reticulospinal neurons labelled by chx10 drive turning through ipsilateral modulation of oscillatory spinal circuits (Cregg et al 2018, Orger et al 2008, Huang et al 2013, Kimura et al 2006). In flies, a recent pan-neuronal imaging study identified the dorsal superior medial protocerebrum (SMP) as a region uniquely correlated with forward velocity (Bresovec et al. 2024). The region houses dendrites of the boltPN, a neuron that can initiate and promote fast forward walking (Bidaye et al. 2020). The SMP neurons labeled in our Throttle-Gal4 line may provide complementary control of a range of walking speeds through graded inhibition. Together these studies suggest that the dorsal SMP may play a role analogous to the vertebrate MLR.

The lateral accessory lobe (LAL) has long been associated with turning behavior in insects (Kanzaki et al. 1994, Namiki and Kanzaki, 2016). The LAL is a major target of outputs of the Central Complex that have been shown to drive goal-directed steering (PFL3 and PFL2, Stone et al. 2017, Hulse et al. 2020, Mussels Pires et al. 2024, Westeinde et al. 2024), and houses DNs whose activity correlates with and drives turning (Rayshubskiy et al. 2020, Yang et al. 2023). In moths, contralaterally-projecting neurons of the LAL have been shown to exhibit "flip-flop" activity that correlates with head movement during pheromone plume tracking (Kanzaki et al. 1994). Previous computational models of the LAL have required this kind of intrinsic rhythmic activity to generate zig-zagging and search at odor offset (Adden et al. 2022, Steinbeck and Graham 2022). While this type of rhythmic activity has not been observed so far in *Drosophila* (Rayshubskiiy et al. 2020, Yang et al. 2023, this study) our model and data suggest that homologous contralaterally projecting neurons may nevertheless play a similar role in controlling the transition between goal-directed steering and search behavior. Comparative studies of these neurons may provide a basis for understanding how species-specific differences in the intrinsic activity of pre-motor neurons influence patterns of search behavior.

How speed and turning are jointly regulated to produce area-restricted search and dispersal behaviors has been most studied in invertebrate species. In larval Drosophila, SEZ neurons have been implicated in modulating the rate of transition between runs and turns (Tastekin et al. 2015). In *c. elegans*, local search is initiated when glutamatergic signaling suppresses activity in two neurons that inhibit local search, AIA and ADE (López-Cruz et al. 2019). In flying flies, a large inhibitory interneuron known as VES041 has recently been identified that suppresses saccades, suggesting it may play a role in shifting behavior from local search to dispersal (Ros et al. 2023). Our statistical analysis of search behavior in walking flies, along with our

computational model and identification of genetic lines that control curvature and walking speed provide insight into the neural control of search behavior in walking flies, and a basis for asking whether neural circuits for area-restricted search, like those for speed control and turning, exhibit conservation across diverse body plans and modes of locomotion.

Acknowledgements

The authors would like to thank Greg Jefferies and Salil Bidaye for helpful suggestions about neural correlates of our models, and Matthew Clark, Claude Desplan, Tom Clandinin, and the Bloomington Drosophila Resource Center for fly lines. Matthieu Louis, Shy Shoham, and Christina Savin, as well as members of the Nagel lab provided feedback on the manuscript. This work was funded by F31 DC019553 to H.G. and R01DC107979 and RF1NS127129 to K.I.N., as well as an NSF neuronex grant (Odor2Action: NSF 2014217) to K.I.N., G.B.E., and J.D.V.

Data and Code Availability

All data and code generated during this study will be made publicly available on Github and Zenodo upon publication.

Materials and Methods

Fly Stocks and Culture

All experimental flies were raised at 25°C on standard cornmeal-agar medium, with a 12h light-dark cycle. All experiments were performed on female flies between 3-8 days old. Genotypes used in each figure were as follows:

Figure 1-2	W^{1118} $norpA^{36}$
Figure 4	VGlut-AD; 31A11-DBD> UAS-Chrimson(III)
Figure 5	VGlut-AD; VT043158-DBD> UAS-Chrimson(III) VGlut-AD; VT043158-DBD> UAS-GtACR1(III)
Figure 6	UAS-PhiC31; VGlut-AD; VT043158-DBD> UAS-Sparc-S-Chrimson (II) UAS-PhiC31; VGlut-AD; VT043158-DBD> UAS-Sparc-I-Chrimson (II)

Experimental flies were collected at least 1 day post eclosion and kept at room temperature in custom made, time-shifted, light boxes for 2-7 days to acclimate to temperature and circadian rhythm. For optogenetic activation, 50 µl all-trans retinal was mixed into ~1 tsp of hydrated potato flakes and added to standard food vials at least four days prior to the experiment. All behavioral experiments were performed between subjective ZT1-ZT4. Flies were starved for ~24 hours before the start of the experiment in empty plastic vials with a dampened Kimwipe for hydration.

A subset of analysis presented here (Figures 1 and 2) use a previously collected dataset of behavioral data from wind tunnel experiments completed using 10% apple cider vinegar. Collection and earlier analysis of these data are described in Alvarez-Salvado et al. 2018 (see Key Resources Table) but followed the same protocols described here.

Wind tunnel experiments

Behavioral experiments in freely-walking flies were performed in miniature wind tunnel arenas as described previously (Álvarez-Salvado *et al*, 2018). Flies were placed in shallow 4cm by 14cm arenas that constrained them to walk. Wind was constant at ~12cm/s. The arenas were backlit with IR LEDS (850nm, Environmental Lights) and monitored from below with a camera (Basler acA1920-155um). Stimuli were controlled through a NIDAQ board. Position and orientation data were collected in real time using custom LABVIEW code.

Flies were run for approximately 2 hours during which they were exposed to 6 randomly interleaved trial types: a blank control trial, a 10 second pulse of 1% apple cider vinegar, light on for the entire 70 seconds, a 10 second light pulse centered in the 70 second trial, a simultaneous 10 s pulse of odor with a 10s pulse of light, and a 10s odor pulse with light on for the entire 70 seconds. Each trial lasted 70 seconds with ~5 seconds between trials. For Chrimson experiments, red light was presented using red LED strips (NFLS-R300X3, SuperBrightLEDs) at 14.6μW/mm^2 for Throttle-gal4 and 15.9μW/mm^2 for Tortuous-gal4 (measured at 625nm). For sparse expression (SPARC) experiments red light was presented at 14.6μW/mm^2. For all GtACR experiments, blue light was presented using blue LED strips (NFLS-B300X3, SuperBrightLEDs) at 36.7μW/mm^2 (measured at 525nm). Previously recorded behavioral responses to odor were recorded using 10% ACV (Alvarez-Salvado et al. 2018). Similar responses were measured to 1% and 10% ACV in that paper.

Walking ball experiments

For walking ball experiments, flies were tethered to an insect pin by the thorax using a small dot of UV-activated glue and placed on an air-supported polypropylene ball (3/8 inch diameter) in a custom 3D printed holder. Airflow supporting the ball was controlled by a flow meter at ~1L/sec. The fly was positioned over the center of the walking ball using a micromanipulator (Thorlabs DT12) and a pipette holder (Sisikyou MXP-8T). Frontal wind at ~10 cm/s (controlled by an Aalborg Model GFC17 mass flow controller) was charcoal-filtered and humidified then delivered to the fly through a 0.175" ID, 0.25" OD nylon tube to encourage walking. The ball was marked with irregular spots to facilitate tracking (Moore et al. 2014) and illuminated using two IR LED fiber optic cables (Thorlabs M118L03 flat cleave patch cables, M850F2 fiber coupled LEDs, and LEDD1B drivers) to the left of the fly. Rotation of the ball was tracked using a Point Grey Camera (90fps, modified 94mm/0.5x InfiniStix Proximity Series lens-approximate working distance of 14.5cm) and FicTrac software (Moore *et al*, 2014, https://github.com/rjdmoore/fictrac). A secondary camera (45fps, Vision Mako U_029B with Edmond Optics 35mm/F1.6 lens) was used to capture video from the side of the fly.

For optogenetic activation, two fiber optic cables (Thorlabs M118L03 flat cleave path cable) were held by clamps (Sisikyou MXB-31), one aimed at the head, 1.5mm in front of the fly's head and 3mm from the ventral nerve cord, and one behind the thorax, 3mm from the ventral nerve cord. Both red and blue light for optogenetic stimulation were produced using fiber coupled LEDs (red: Thorlabs M617F2, blue: Thorlabs M470F3) controlled by Thorlabs LEDD1B drivers. During each 100s long trial, flies were presented with 30 seconds of light stimulation, centered in 90 seconds of wind. We used 6 different light intensity levels that were presented in random order and set using a voltage input to the LED driver. The voltages chosen were 5, 2.5, 1, 0.5, 0.25 and 0.1V. The resultant light intensities for red light stimulation were: 22.9, 11.3, 4.2, 2.1, 0.9, and 0.3 μW/mm^2 (measured at 625nm). The resultant light intensities for blue light stimulation were: 25,13.4, 5.5, 2.8, 1.4, and 0.4 μW/mm^2 (measured at 525nm). For each light intensity we ran 5 consecutive trials of the same intensity. All light intensities were presented from one fiber before the other, with the order of fiber presentation pseudorandom across flies. Custom Python code was used to control stimulus presentation and data collection (GITHUB) via a NIDAQ board and an Arduino (GITHUB).

Electrophysiology

Whole-cell patch clamp electrophysiology experiments were performed from LAL neurons in 2–5-day old female flies expressing *UAS-GFP* under the Throttle-Gal4 expression pattern. Flies were briefly cold anesthetized, head and thorax were mounted onto a custom stage and securely adhered to the stage using UV glue. A small imaging window was cut into the cuticle of the flies' head using sharp forceps while perfusing oxygenated Drosophila AHLS (103 mM NaCl, 3 mM KCl, 5 mM TES, 8 mM trehalose dihydrate, 10 mM glucose, 26 mM $NaHCO_3$, 1 mM $NaH_2PO_4H_20$, 1.5 mM $CaCl_22H_2O$, and 4 mM $MgCl_26H_2O$, pH 7.1–7.4, osmolarity 270–274 mOsm) over the open head capsule. Throughout the experiment the imaging window was under a constant flow perfusion of oxygenated Drosophila AHLS solution using carbogen (95% oxygen, 5% carbon dioxide). Brain regions and cell bodies of interest were visualized within the open head capsule using a 40x objective (Olympus, LUMPLFLN40XW) and illuminated using a Cairn Research MonoLED system in addition to an IR LED fiber optic (ThorLabs #MF850F2) placed posterior to the fly (~1-4 cm away). Cell bodies were cleaned using slight positive from a glass pipette (World Precision Instruments TW150F-3) filled with extracellular saline. Recordings were made with glass patch pipettes (World Precision Instruments 1B150F-3) pulled to 2-10 MOhms using a Sutter P-1000 puller. Patch pipettes were filled with internal saline solution: 140 mM KOH, 140 mM aspartic acid, 10 mM HEPES, 1 mM EGTA, 1 mM KCl, 4 mM MgATP, 0.5 mM Na3GFP, and 13 mM biocytin hydrazide. Current and voltage signals were amplified using a Brownlee Precision 410 preamplifier and Molecular Devices Axopatch 200B, and digitized at 10 kHz. For analysis, spikes were sorted and down-sampled to 1KHz, then smoothed with a 500ms hanning window to compute peri-stimulus time histograms. We recorded 8 flies that met an access:input ratio of ~5:1 or greater. A brief hyperpolarizing pulse was injected into the cell at the start of each trial to measure input resistance. Activity was measure using the firing rate from the remainder of the 6 second trial following this pulse.

Throughout the experiment, flies were exposed to air flow at a rate of ~1L/min. An olfactory stimulus of 1% Apple Cider Vinegar was delivered using a custom-built olfactometer constructed of a charcoal filter, solenoid valve (Lee company, LFAA1201610H) and Teflon tube placed less than 1 cm directly in front of the fly. Flow rate was kept constant using a compensatory solenoid valve (Lee company, LFAA1201610H). Flies were exposed to 2 seconds of odor stimulus preceded by 2 seconds of baseline air exposure and followed by 2 seconds of air post-exposure.

Immunohistochemistry and imaging

Brains were dissected in PBS and then fixed for 14 minutes in 4% paraformaldehyde in PBS. After fixing, brains were washed 3 times in PBS and stored at 4°C until staining (≤1 week). Brains were incubated in 5% normal goat serum in PBST (0.2% Triton-X in 1x PBS) for a minimum of 60 minutes and then incubated overnight in primary antibody. Brains were then washed 3x with PBST and incubated overnight in secondary antibody. Brains were washed 3x in PBST, then mounted, covered in vectasheild (Vector Labs H-1000) and enclosed with a coverslip prior to imaging with a 20x objective (Zeiss W Plan-Apochromat 20x/1.0 DIC CG 0.17 M27 75mm) on a Zeiss LSM 800 confocal microscope at 1.25 µm depth resolution. All images were created in Image J using a maximum z-projection. Antibodies used were as follows:

Antibodies	**Source**	**Dilution**	**Identification**
Mouse anti-nc82	DSHB	1:50	RRID: AB_2314866
Chicken anti-GFP	Fisher Scientific	1:50	RRID: AB_1074893
Rabbit anti-DsRed	Clontech	1:500	RRID: AB_477652
Rabbit anti-VGlut	A. DiAntonio lab	1:1000	

Alexa488-conjugated goat anti-chicken	Fisher Scientific	1:250	RRID: AB_2534096
Alexa633-conjugated goat anti-mouse	Fisher Scientific	1:250	RRID: AB_2535719
Alexa568-conjugated goat anti-rabbit	Fisher Scientific	1:250	RRID: AB2315774

Data Analysis

Analysis of Behavioral Data

All analysis was performed in MATLAB (Mathworks, Natick, MA).

Analysis of wind tunnel data

For wind tunnel experiments, individual trials were excluded due to tracking error or if flies did not move a minimum distance of 25mm over the duration of the trial. For angular velocity autocorrelogram computations, raw data (both new and from previous publications) were re-imported without low-pass filtering. For other analyses, position and orientation data were low-pass filtered at 2.5 Hz using a 2-pole Butterworth filter prior to subsequent analysis. Movement parameters including ground speed and angular velocity were computed from centroid position and orientation measurements as described previously (Alvarez-Salvado et al. 2018).

Histograms of ground speed or angular velocity were computed for each fly based on data during the first 10 seconds of baseline or post-odor periods of all trials. Data shown represent the mean and standard error across flies. Angular velocity autocorrelograms were computed from the first 10 seconds of baseline and post-odor periods of all trials. Here, raw (unfiltered) angular velocity measurements for each fly were mean-subtracted and the autocorrelogram was computed using the MATLAB function 'xcorr' normalized to one at zero lag. Data shown represent the mean and standard error across flies.

To compute angular dispersion, the initial heading was subtracted from the unwrapped orientation for each time period (baseline or post-odor period) and the absolute value was taken. Data shown represent mean and standard error across flies as a function of time since the start of that period. To compute inter-turn interval distributions, turns were detected using positive threshold crossings at 45 deg/sec in the absolute angular velocity trace. Turn times were used to compute inter-turn intervals.

To segment ground speed into epochs of different means, we used a change point detection algorithm (Matlab's 'findchangepts') with a minimum distance of 100 samples and a minimum threshold for residual error improvement of 1000. To analyze odor-evoked trajectories as a function of initial behavioral state, we examined the mean ground speed as determined by this algorithm in the 2 seconds before the onset of the odor stimulus. We used this value to categorize trails into 'moving' or 'not moving' using a threshold of 1mm/s. Length of path was calculated as the cumulative sum of the cartesian distance between subsequent samples within a trial.

To measure interactions between turning and groundspeed, we first detected turns as positive threshold crossings in the absolute angular velocity at 45 degrees/s, and extracted turns as the period from 0.5 seconds before to 0.7 seconds after this threshold crossings. We used the mean ground speed in the first 0.5 seconds of our extracted windows to sort both ground speed and angular velocity windows into 6 categories (<1mm/s, 1-3mm/s, 3-8mm/s, 8-12mm/s, 12-18mm/s and >18mm/s). We then calculated the mean and standard error of groundspeed and angular velocity within each category.

For the cross-correlation of model units, unit activity was mean-subtracted and the cross-correlation was calculated using Matlab's 'xcorr' function using the 'coeff' flag for normalization.

Analysis of walking ball data

For walking ball data, rotation in the pitch and yaw directions were extracted from FicTrac output and used as forward and angular velocity, respectively. (Thus, we report forward velocity for walking ball data as opposed to ground speed for freely walking wind tunnel data.) These outputs were processed by smoothing over a 1 second window (MATLAB 'smooth' function). Time course data represent the mean and standard error of forward or angular velocity across flies for the time period and light intensity shown. To calculate the change in angular velocity and forward velocity in response to light stimuli at different light levels, we took the mean parameter value across the 30 seconds of light stimulation and subtracted the mean value across the 30 seconds preceding light stimulation. Data shown represent the mean and standard error across flies.

Analysis of SPARC data

For sparse expression experiments, flies expressing either 5% or 15% Chrimson SPARC constructs under the Throttle-Gal4 driver were individually run in our wind tunnel apparatus as described above. After data collection, flies were anesthetized using carbon dioxide and collected for dissection, maintaining the arena identity of each fly. Individual brains were fixed, stained, and imaged as described above. Anatomical data were blindly scored by two human observers (H.G. and B.d.l.R). into the following categories: SMP neurons, dorsal LAL neurons, medial LAL neurons, ventral LAL neurons, and other. SMP neurons were defined as those with cell bodies along the dorsal midline of the brain, with processes in SMP projecting down, along the midline. Dorsal LAL neurons were defined as those whose processes reside in the LAL and project contralaterally via the more dorsal decussation seen in the Throttle-Gal4 population. Medial and ventral LAL neurons were defined as neurons whose processes reside in the LAL and decussate through the more ventral decussation seen in the overall population. The bottom of the antennal lobe was used to demarcate these two populations. Neurons whose processes extended beyond the bottom of the antennal lobe were classified as ventral and those that didn't were referred to as medial. All neurons that did not fall within the predetermined categories were classified as 'other'.

To perform principal component analysis on behavior, the mean ground speed and angular velocity response to optogenetic activation were calculated for each fly. For each fly, mean ground speed and angular velocity were normalized by subtracting the overall mean each signal, respectively, and dividing its standard deviation before being concatenated into a response vector. Principal components analysis was performed on the matrix of response vectors for each fly. Response vectors were projected onto the first two principal components and plotted against anatomical data for each fly.

Model construction and analysis

All modeling was performed in MATLAB. Our model of locomotor control was based on two layers. In the first layer, 5 units (u_{1-5}), receive independent Gaussian noise and interact through a matrix of synaptic weights. The activity of each unit evolves according to:

$$\vec{u}(t+\Delta t) = a(M\vec{u}(t) + \vec{\omega}(t)) \quad (1)$$

where $\Delta t = 20ms$, equivalent to our sampling rate for behavioral data, M is a matrix of weights, $\vec{\omega}$ is a Gaussian noise term, and *a* is a sigmoid function that keeps activity bounded:

$$a(x) = \frac{20}{1+e^{-x/4}} - 10 \quad (2)$$

The weight matrix M has positive values along the diagonal, corresponding to auto-regressive terms A, and two negative parameters corresponding to stop inhibition (I_s, mutual inhibition between u_3 and all other units) and contralateral inhibition (I_c, mutual inhibition between left $u_{1,2}$ and right $u_{4,5}$ movement-producing units):

$$M = \begin{bmatrix} A & 0 & I_s & I_c & I_c \\ 0 & A & I_s & I_c & I_c \\ I_s & I_s & A & I_s & I_s \\ I_c & I_c & I_s & A & 0 \\ I_c & I_c & I_s & 0 & A \end{bmatrix} \tag{3}$$

In the version of the model shown, $A = 0.8$, $I_s = -0.03$, $I_c = -0.015$ at baseline and $I_c = -0.025$ during offset search.

In the second layer, locomotor parameters (forward and angular velocity) are computed based on the activity of all units, according to the following equations:

$$\begin{aligned} &\text{if } u_3 \geq 0 && v = 0,\ \dot{\theta} = 0 \\ &\text{if } u_3 < 0 && v = \alpha \max(0, u_1 + u_5) + \beta \max(0, u_2 + u_4) \\ & && \dot{\theta} = \gamma(u_1 - u_5) + \delta(u_2 - u_4) \end{aligned} \tag{4}$$

Where v and $\dot{\theta}$ are forward and angular velocity and the parameters $\alpha, \beta, \gamma, \delta$ set the gain of forward and angular velocity for each pair of units:

α	1.6 mm/sample
β	0.5 mm/sample
γ	0.2 °/sample
δ	0.35 °/sample

To generate sharper large turns we introduced a gain term on forward velocity that reduces speed during large turns:

$$v_{out} = g[\alpha \max(0, u_1 + u_5) + \beta \max(0, u_2 + u_4)] \tag{5}$$

where $g = 1$ if $|\dot{\theta}| \leq 3$

$g = \sqrt{\frac{3}{|\dot{\theta}|}}$ if $|\dot{\theta}| > 3$

In order to model odor effects on behavior, we introduced two odor-gated terms that impact unit activity. In the presence of odor, we added a negative offset to the stop unit to suppress its activity:

$$S_{stop} = [0\ 0 - 0.1\ 0\ 0]' \tag{6}$$

In addition, a steering function proportional to the sine of the difference between the current heading (θ) and the wind angle (ψ) was added to the activity of the movement producing units:

$$S(t) = [1\ 1\ 0 - 1 - 1]' sin(\theta(t) - \psi) \tag{7}$$

Both terms were added to the unit activity as follows:

$$\vec{u}(t + \Delta t) = a\big(M\vec{u}(t) + S(t) + S_{stop}(t) + \vec{\omega}(t)\big) \tag{8}$$

To model the effect of feedforward inhibition and activation in our model, we added a tonic offset $T(t)$ to activity across all units:

$$\vec{u}(t+\Delta t) = a\big(M\vec{u}(t) + S(t) + S_{stop}(t) + T(t) + \vec{\omega}(t)\big) \quad (9)$$

See attached appendix for detailed analysis of the model.

Connectomics

Connectomic data from hemibrain v1.2.1 were obtained from neuprint (https://neuprint.janelia.org, hemibrain:v1.2.1) using custom queries and organized and analyzed in Microsoft Excel. The VGlut-AD;31A11-DBD population was identified as LAL091-LAL095. The VGlut-AD;VT043158-DBD population was identified as LAL073-074 and LAL120-126. We counted recurrent synapses between neurons within our identified populations, synapses from MBONs and PFL neurons onto our identified populations, and synapses from our identified populations onto DNs. We also identified connections between VGlut-AD;31A11-DBD population and AOTU neurons, as well as di-synaptic connections between the LAL090-LAL095 population and DNs through AOTU neurons. Synaptic weights less than 3 were excluded.

Key Resources Table

Resource	**Source**	**Identifier**
FLY LINES		
VGlut-AD	BDSC	RRID:BDSC_84713
VT043158-DBD	BDSC	RRID:BDSC_73583
31A11-DBD	BDSC	RRID:BDSC_69813
UAS-Chrimson	BDSC	RRID:BDSC_55136
w1118; s/Cyo; UAS-GtACR1-EYFP/TM6b	Claude Desplan	
10X UAS-CD8:GFP	BDSC	RRID:BDSC_32183
U.F.C/yshid;LexAop-Flp/[cyo];Gad1-LexA/[TM3]	Matthew Clark	
U.F.C/yshid;LexAop-Flp/[cyo];Chat-LexA/[TM3]	Matthew Clark	
20XUAS-IVS-phiC31(x)	BDSC	RRID:BDSC_84153
20XUAS-Sparc2-I-Syn21-CsChrimson::tdTomato	Tom Clandinin	RRID:BDSC_84144
20XUAS-Sparc2-S-Syn21-CsChrimson::tdTomato	Tom Clandinin	RRID:BDSC_84145
REAGENTS		

All trans retinal	Sigma	RRID: R2500
SOFTWARE		
Python		Version 3.8
MATLAB	Mathworks	Version R2023a
Image J		Version 1.53t
Microsoft Excel		Version 2308
FicTrac		Version 2.0 (build date: Nov 2 2018)
DATASETS		
hemibrain connectome	https://neuprint.janelia.org/	Version: v1.2.1
Data from Alvarez-Salvado et al. 2018	https://doi.org/10.5061/dryad.g27mq71	

Appendix: Locomotion Control Model

This appendix provides an approximate analytic treatment of the model of locomotion control presented in the body of the manuscript, with the goal of providing insights into the model's behavior and its dependence on parameters.

The primary result is that the model can be broken into two components ("symmetric" and "antisymmetric") that separately control forward velocity and angular velocity, and are differentially impacted by the control signals related to odor and wind that we introduce. The dynamic characteristics of the antisymmetric component are directly manifest in the tortuosity of the trajectories produced by the model and are controlled by the eigenvalues of that component, with a positive eigenvalue leading to unstable behavior and more tortuous trajectories. We find that when self-excitation is set close to the border between stable and unstable behavior, the level of contralateral inhibition can more readily and smoothly impact tortuosity – an observation that motivates our choice of parameters in the main paper. Finally, we show that the model exhibits similar dynamics regardless of the number of locomotor units on each side, so long as the symmetries of the connectivity matrix are preserved.

A more detailed outline is as follows. We begin by showing that for small signals, the model can be approximated by a linear differential equation for a five-dimensional vector of unit activities. The five-dimensional model splits into a three-dimensional symmetric part that is concerned with forward velocity and a two-dimensional antisymmetric part that is concerned with angular velocity, and this splitting is exact for the linearized approximation. As they are linear, both of these components have a single fixed point. Depending on parameter values, the fixed points of the two subsystems can be stable, neutrally stable, or unstable, and we determine the parameter values at which these transitions occur. (In the unstable regime, activity is nevertheless bounded, because of the model's sigmoidal activation function). For the antisymmetric subsystem, the stable regime produces trajectories are straighter than what is observed experimentally. Parameters that lead to a slightly unstable fixed point provide good matches for experimental data by producing periods of consistent turning in one direction or the other. Increasing the strength of self-excitation or contralateral inhibition pushes the fixed point of the antisymmetric component further into instability, further elongating the periods of consistent turning to a duration that results in trajectories that are too curved to match experimental data. While increasing the strength of self-excitation or stop-inhibition can also lead to instability, it does not create the observed turning behavior, and the analysis shows why this is the case: these destabilizing influences primarily affect the symmetric subsystem, which controls forward but not angular velocity. Finally, we show that the model's behavior is preserved with either more, or fewer, units on each side. Specifically, changing the number of units has the same effect on stability characteristics as changing the per-connection strength of the inhibitory signals.

Linearization and conversion from difference equation to differential equation

The model equation of the main text can be rewritten as

$$\vec{u}(t+\Delta t) = a(M\vec{u}(t) + \vec{s}(t)), \tag{1}$$

where $\vec{u}(t)$ is the column vector $\begin{bmatrix} u_1(t) & u_2(t) & u_3(t) & u_4(t) & u_5(t) \end{bmatrix}'$, M is a 5×5 matrix of coupling constants (see Fig. 3C and text equation 3), $\vec{s}(t)$ is a driving signal, and $a(x)$ is a sigmoidal activation function to be applied element-by-element to its column-vector argument. Reproducing eq. (3) of the main text,

$$M = \begin{bmatrix} A & 0 & I_S & I_C & I_C \\ 0 & A & I_S & I_C & I_C \\ I_S & I_S & A & I_S & I_S \\ I_C & I_C & I_S & A & 0 \\ I_C & I_C & I_S & 0 & A \end{bmatrix}, \tag{2}$$

where $A = 0.8$, $I_S = -0.03$, and $I_C = -0.015$ at baseline and $I_C = -0.025$ at odor offset.
The driving signal $\vec{s}(t)$ consists of independent Gaussian noise ($\vec{\omega}$ in the main text), to which exogenous signals due to odor, wind, and activation (text equations 6, 7, and 9) may be added. The activation function is specified by text equation (2), and may be rewritten as

$$a(x) = a_0 \left(\frac{2}{1+e^{-2x/a_1}} - 1 \right) = a_0 \left(\frac{e^{x/a_1} - e^{-x/a_1}}{e^{x/a_1} + e^{-x/a_1}} \right) = a_0 \tanh(\frac{x}{a_1}), \tag{3}$$

with $a_0 = 10$ and $a_1 = 8$. Note that when its inputs are small, the activation function is approximately linear:

$$a(x) = \frac{a_0}{a_1} x + O(x^3), \tag{4}$$

an approximation that is useful when $|x| \ll a_1$.

The model equation (1) is equivalent to

$$\frac{\vec{u}(t+\Delta t) - \vec{u}(t)}{\Delta t} = \frac{1}{\Delta t} \left(a(M\vec{u}(t) + \vec{s}(t)) - \vec{u}(t) \right). \tag{5}$$

Assuming that Δt is small compared to the time course of input fluctuations ($\Delta t = 20$ ms in the implementation of eq. (1)), and that the inputs are sufficiently small so that eq. (4) can be used, eq. (5) is approximated by

$$\frac{d}{dt}\vec{u}(t) = L\vec{u}(t) + \frac{1}{\Delta t}\frac{a_0}{a_1}\vec{s}(t), \tag{6}$$

where

$$L = \frac{1}{\Delta t}\left(\frac{a_0}{a_1} M - I \right). \tag{7}$$

Thus, L is a 5×5 matrix with the same symmetry as M,

$$L = \begin{bmatrix} k_E & 0 & -k_S & -k_C & -k_C \\ 0 & k_E & -k_S & -k_C & -k_C \\ -k_S & -k_S & k_E & -k_S & -k_S \\ -k_C & -k_C & -k_S & k_E & 0 \\ -k_C & -k_C & -k_S & 0 & k_E \end{bmatrix}, \tag{8}$$

where the constants k_E (self-excitation), k_S (stop-inhibition), and k_C (contralateral inhibition) are related to the quantities in the main text by

$$k_E = \frac{1}{\Delta t}\left(\frac{a_0}{a_1} A - 1 \right); \; k_S = -\frac{1}{\Delta t}\frac{a_0}{a_1} I_S; \; k_C = -\frac{1}{\Delta t}\frac{a_0}{a_1} I_C. \tag{9}$$

Importantly, for the parameter values considered in the main text ($A = 0.8, a_0 = 10$ and $a_1 = 8$), eq. (9) shows that the self-excitation strength $k_E = 0$. That is, the level of recurrent excitation postulated in the difference-equation formulation of the main text does not require an explicit recurrent connection at all, and corresponds to units which, if unperturbed, maintain their activity level over time.

Note also that the constants k_S and k_C are positive for the range of values of parameters considered in the main text; positive values indicate inhibition because of the minus sign in eq. (8).

As in Fig. 3B of the main text, the activities $\vec{u}$ result in locomotion whose forward and angular velocities are given by

$$\begin{aligned} &If\ u_3(t)<0: \begin{array}{l} v(t)=\alpha\left(u_1(t)+u_5(t)\right)+\beta\left(u_2(t)+u_4(t)\right) \\ \dot{\theta}(t)=\gamma\left(u_1(t)-u_5(t)\right)+\delta\left(u_2(t)-u_4(t)\right) \end{array} \\ &If\ u_3(t)\geq 0: \begin{array}{l} v(t)=0 \\ \dot{\theta}(t)=0 \end{array} \end{aligned}, \tag{10}$$

where α, β, γ, and δ are specified in the text.

Splitting the system

The full model is five-dimensional, but the symmetry of the coupling matrix L (eq. (8)) allows for a splitting of the model via a coordinate rotation:

$$\vec{q}=R\vec{u}\,, \tag{11}$$

where

$$R=\begin{bmatrix} \frac{1}{\sqrt{2}} & 0 & 0 & 0 & \frac{1}{\sqrt{2}} \\ 0 & \frac{1}{\sqrt{2}} & 0 & \frac{1}{\sqrt{2}} & 0 \\ 0 & 0 & 1 & 0 & 0 \\ -\frac{1}{\sqrt{2}} & 0 & 0 & 0 & \frac{1}{\sqrt{2}} \\ 0 & -\frac{1}{\sqrt{2}} & 0 & \frac{1}{\sqrt{2}} & 0 \end{bmatrix}, \tag{12}$$

is a rotation matrix, satisfying $R^{-1}=R^T$. In the new coordinates, the model (eq. (6)) becomes

$$\frac{d}{dt}R^{-1}\vec{q}(t)=LR^{-1}\vec{q}(t)+\vec{s}(t)\,, \tag{13}$$

which is equivalent to

$$\frac{d}{dt}\vec{q}(t)=L_{rot}\vec{q}(t)+R\vec{s}(t)\,, \tag{14}$$

with $L_{rot}=RLR^{-1}$. As expected from the symmetry-based transformation of model variables, the transformed coupling matrix L_{rot} is block-diagonal:

$$L_{rot}=RLR^{-1}=R\begin{bmatrix} k_E & 0 & -k_S & -k_C & -k_C \\ 0 & k_E & -k_S & -k_C & -k_C \\ -k_S & -k_S & k_E & -k_S & -k_S \\ -k_C & -k_C & -k_S & k_E & 0 \\ -k_C & -k_C & -k_S & 0 & k_E \end{bmatrix}R^{-1}=\begin{bmatrix} k_E-k_C & -k_C & -k_S\sqrt{2} & 0 & 0 \\ -k_C & k_E-k_C & -k_S\sqrt{2} & 0 & 0 \\ -k_S\sqrt{2} & -k_S\sqrt{2} & k_E & 0 & 0 \\ 0 & 0 & 0 & k_E+k_C & k_C \\ 0 & 0 & 0 & k_C & k_E+k_C \end{bmatrix}, \tag{15}$$

Eq. (15) shows that the transformation of the original model (eq. (6)) into rotated variables (eq. (14)) splits the original system into a three-dimensional part in which the original variables are combined

symmetrically, and a two-dimensional part in which they combine antisymmetrically. We make this split explicit, with $\vec{y}$ the three-dimensional symmetric part, and $\vec{z}$ the two-dimensional antisymmetric part:

$$\vec{q}(t)=\begin{bmatrix}\vec{y}(t)\\ \vec{z}(t)\end{bmatrix}: \quad y_1=\frac{1}{\sqrt{2}}(u_1+u_5),\ y_2=\frac{1}{\sqrt{2}}(u_2+u_4),\ y_3=u_3,\ z_1=\frac{1}{\sqrt{2}}(-u_1+u_5),\ z_2=\frac{1}{\sqrt{2}}(-u_2+u_4), \tag{16}$$

The original system is now approximated by

$$\begin{aligned}\frac{d}{dt}\vec{y}(t)&=L_{sym}\vec{y}(t)+\vec{s}_{sym}(t)\\ \frac{d}{dt}\vec{z}(t)&=L_{anti}\vec{z}(t)+\vec{s}_{anti}(t)\end{aligned}, \tag{17}$$

where

$$L_{sym}=\begin{bmatrix}k_E-k_C & -k_C & -k_S\sqrt{2}\\ -k_C & k_E-k_C & -k_S\sqrt{2}\\ -k_S\sqrt{2} & -k_S\sqrt{2} & k_E\end{bmatrix},\ L_{anti}=\begin{bmatrix}k_E+k_C & k_C\\ k_C & k_E+k_C\end{bmatrix}, \tag{18}$$

and $\vec{s}_{sym}(t)$ and $\vec{s}_{anti}(t)$ are the first three, and the last two, dimensions of $R\vec{s}(t)$.

This splitting simplifies the analysis of the model's driving signals and locomotor outputs. Since the transformation R is a rotation, the noise component of $\vec{s}(t)$, which is assumed to be a set of uncorrelated Gaussian noises, remains uncorrelated and Gaussian when split into $\vec{s}_{sym}(t)$ and $\vec{s}_{anti}(t)$. The other model inputs selectively activate either the symmetric or antisymmetric components. The stop signal, $c_{stop}\begin{bmatrix}0 & 0 & -1 & 0 & 0\end{bmatrix}'$ (main text eq. 6) splits into a symmetric component $c_{stop}\begin{bmatrix}0 & 0 & -1\end{bmatrix}'$ and an antisymmetric component of 0. The wind-related signal, $\sin(\theta(t)-\psi)\begin{bmatrix}1 & 1 & 0 & -1 & -1\end{bmatrix}'$ (main text eq. 7) splits into a symmetric component of 0 and an asymmetric component of $-\sqrt{2}\sin(\theta(t)-\psi)\begin{bmatrix}1 & 1\end{bmatrix}'$. Tonic activity $c_{tonic}(t)\begin{bmatrix}1 & 1 & 1 & 1 & 1\end{bmatrix}'$ splits into a symmetric component $c_{tonic}(t)\begin{bmatrix}\sqrt{2} & \sqrt{2} & 1\end{bmatrix}'$ and an antisymmetric component of 0. In terms of the new variables of eq. (17), the locomotor outputs (10) become

$$\begin{aligned}&If\ \ y_3(t)<0: \begin{aligned}v(t)&=\sqrt{2}\left(\alpha y_1(t)+\beta y_2(t)\right)\\ \dot{\theta}(t)&=-\sqrt{2}\left(\gamma z_1(t)+\delta z_2(t)\right)\end{aligned}\\ &If\ \ y_3(t)\geq 0: \begin{aligned}v(t)&=0\\ \dot{\theta}(t)&=0\end{aligned}\end{aligned}. \tag{19}$$

That is, the forward velocity signal only depends on the output of the symmetric component, and the angular velocity signal only depends on the output of the antisymmetric component. In the linearized approximation, the only coupling of these signals occurs when they are translated into movement: the stop signal (which is part of the symmetric component) vetoes both forward velocity and angular velocity, and the "gating" equation (main text eq. 5) by which angular velocity modulates forward velocity.

Finally, note that the symmetry-based splitting remains useful even when the small-signal linearizing approximation $\tanh x\approx x$ used in eq. (4) does not hold, since the sigmoidal compression respects this

symmetry: $\tanh(-x) = -\tanh(x)$. Consequently, a model state in which activity confined to the symmetric component will remain confined to that component and generate no activity in the antisymmetric component, and vice-versa.

Fixed-point behavior

As is standard, we analyze the qualitative behavior of the systems given by eq. (17) in terms of the presence of fixed points and the behavior of model dynamics at the fixed points. Since each of these systems is a linear differential equation with constant coefficients, they each have a single fixed point, at the origin. Moreover, since the matrices in eq. (18) are real and symmetric (and non-singular), their full set of solutions are sums of exponentials $\sum_m \vec{x}_m e^{\lambda_m t}$, where the constants λ_m are the eigenvalues of the matrices L_{sym} and L_{anti}, and $\vec{x}$ is a two- or three-dimensional column eigenvector. These eigenvalues determine the qualitative behavior of the equations' solutions, and the system's responses to pulse inputs. If all eigenvalues are negative, all solutions tend to zero and the fixed point is stable; if any λ_m is positive, then there are solutions $\vec{x}_m e^{\lambda_m t}$ that will depart from the fixed point exponentially. In the full model, this exponential departure will continue until the linearized approximation is no longer valid, at which point the saturation of the sigmoidal activation function will keep the solution bounded.

The eigenvectors and eigenvalues for both subsystems are readily determined (below). In both cases, since the matrices L_{sym} and L_{anti} are real and symmetric, their eigenvalues must be real and their eigenvectors must be orthogonal.

Symmetric component

For L_{sym}, $\begin{bmatrix}1 & -1 & 0\end{bmatrix}'$ is evidently an eigenvector, with eigenvalue $\lambda_E = k_E$. The other eigenvectors, since they must be orthogonal to $\begin{bmatrix}1 & -1 & 0\end{bmatrix}'$, are of the form $\vec{h} = \begin{bmatrix}1 & 1 & h\end{bmatrix}'$.

To determine h, note that if $\vec{h}$ is an eigenvector, then $L_{sym}\vec{h}$ must be proportional to $\vec{h}$, so the third element of

$$L_{sym}\vec{h} = \begin{bmatrix} k_E - 2k_C - hk_S\sqrt{2} \\ k_E - 2k_C - hk_S\sqrt{2} \\ -2k_S\sqrt{2} + hk_E \end{bmatrix} \tag{20}$$

must be h times as large as each of the first two elements. This requires

$$-2k_S\sqrt{2} + hk_E = h\left(k_E - 2k_C - hk_S\sqrt{2}\right), \tag{21}$$

a quadratic equation whose roots are given by

$$h_\pm = \frac{1}{\sqrt{2}}\left(\frac{-k_C \mp \sqrt{k_C{}^2 + 4k_S{}^2}}{k_S}\right). \tag{22}$$

With these choices, $L_{sym}\vec{h}_\pm = \lambda_\pm \begin{bmatrix}1 & 1 & h_\pm\end{bmatrix}'$. So the two remaining eigenvalues $\lambda_\pm$ can be read off from the first entry of $L_{sym}\vec{h}_\pm$ on the right-hand side of eq. (20):

$$\lambda_\pm = k_E - 2k_C - h_\pm k_S\sqrt{2} = k_E - k_C \pm \sqrt{k_C{}^2 + 4k_S{}^2}\ . \tag{23}$$

Thus, the symmetric component has one eigenvalue at k_E, and two eigenvalues equally-spaced above and below $k_E - k_C$, with the more positive value (λ_+ in eq. (23)) always greater than k_E. So if $k_E > 0$, at least

two eigenvectors determine unstable trajectories ($\lambda_E = k_E$ and λ_+ in eq. (23)). Conversely, $k_E < 0$ is required for stability. However, even if $k_E < 0$, there is always a larger eigenvalue, λ_+, and it too must be negative to ensure stability. That is, the symmetric component's fixed point is only stable when $k_E < 0$ and $\lambda_+ < 0$, which in turn requires that

$$k_C > \frac{k_E^2 - 4k_S^2}{2k_E}. \tag{24}$$

In terms of the parameters in the main text, $k_E = 0$ when $A = \frac{a_1}{a_0} = 0.8$ (per eq. (9)), so the condition that $k_E < 0$ is equivalent to $A < \frac{a_1}{a_0} = 0.8$. The condition (24), in terms of the model parameters of the main text, is

$$I_C < \frac{1}{2} \frac{4I_S^2 - \left(A - \frac{a_1}{a_0}\right)^2}{A - \frac{a_1}{a_0}}. \tag{25}$$

Antisymmetric component

The antisymmetric component determines the model's turning behavior, and it has a simpler structure than the symmetric component. The form of the 2×2 matrix L_{anti} makes both eigenvectors evident: $\begin{bmatrix} 1 & 1 \end{bmatrix}'$, with eigenvalue

$$\lambda_{E+2C} = k_E + 2k_C, \tag{26}$$

and $\begin{bmatrix} 1 & -1 \end{bmatrix}'$ with eigenvalue $\lambda_E = k_E$. Both eigenvectors result in consistent turning in a single direction, but the $\begin{bmatrix} 1 & 1 \end{bmatrix}'$ eigenvector will result in a greater angular velocity since the two terms that contribute to $\dot{\theta}$ in eq. (19) will reinforce.

When k_E is negative (i.e., $A < \frac{a_1}{a_0} = 0.8$) and $k_E + 2k_C < 0$, the sole fixed point at the origin is stable. Thus, in terms of the model parameters of the main text, the fixed point of the antisymmetric component is stable when

$$A - 2I_C < \frac{a_1}{a_0}. \tag{27}$$

In this regime, perturbations due to a driving signal (e.g., random noise) around the fixed point of zero will lead to activity that returns to zero, with a rate constant given by the eigenvalue that is closest to zero. As a result, this regime will not have by prolonged periods of turning in one direction.

In the unstable regime (when the inequality in eq. (27) is reversed), behavior contrasts markedly. Perturbations around the fixed point will lead to activity that diverges until it limited by the sigmoid activation function of the full model, or driven back to zero by another perturbation. Thus, this regime will be characterized by prolonged periods of turning in one direction, or the other. The duration of these periods will be influenced by the extent of instability of the fixed point: with greater instability, the activity variables will be driven more strongly towards the limits of the sigmoid, and perturbations that suffice to drive them back to zero will be increasingly rare. As increasing k_C leads to greater instability, this behavior will be accentuated as k_C

increases (i.e., as I_C becomes more negative). As shown by the simulations in the body and below, only slight instability is required to account for the level of turning observed experimentally.

Model regimes

Figure S3 illustrates how the locomotion trajectories depend on A and I_C for a range of values around the parameters chosen in the main text and that straddle the values at which the fixed points change their behavior. For $A = 0.7$ (top row), the fixed point of the antisymmetric component is stable for $I_C \geq -0.005$ (first four panels with baseline and offset parameters, and fifth panel with baseline parameters). Under these circumstances, the trajectories are straighter than experimentally observed. For $A = 0.9$ (bottom row), the antisymmetric fixed point is unstable, and becomes progressively more so as I_C becomes more negative (from left to right). These trajectories have tight corkscrew components, which are not observed experimentally. For $A = 0.8$ (middle row), for values of I_C in the range -0.015 to -0.035, the models produce trajectories with modest curvature, consistent with experimental data. These parameters yield a fixed point that is slightly unstable. Similar trajectories are also seen in the rightmost panels of the top row, where also, the fixed point of the antisymmetric component is also slightly unstable. However, the underlying dynamics are quite different, because the fixed point of the symmetric component is stable. Consequently, there are no sustained periods in which the stop unit is active vs. inactive – so in this regime, the model fails to predict the experimentally-observed stops in the trajectory.

Role of the instability generated by contralateral inhibition

The analysis above shows that in the absence of contralateral inhibition, instability generated by stop inhibition or self-excitation cannot substitute as an explanation for trajectory curvature. Without contralateral inhibition (i.e., when $k_C = I_C = 0$), instability can be generated when $k_E > 0$ (corresponding to $A > 0.8$) or when k_S is sufficiently positive (I_S sufficiently negative), as shown by eqs. (23) and (25). However, this instability will not generate prolonged periods of turning in one direction, as the instability has its origin in the symmetric subsystem. Specifically, dynamics will fluctuate between periods in which there are extremes of activity in the symmetric subsystem (stop unit quiescent and other units active, or occasionally stop unit active and other units quiescent), but, since $I_C = 0$, there won't be any tendency for bilaterally-paired units to be out of phase. Consequently, the swings of activity in the stop unit will interrupt periods of large forward velocity and periods of turning, but those periods of turning will have directions that fluctuate around zero, rather than maintained in one or the other direction.

Note also that a self-excitation value of zero ($k_E = 0$, or $A = 0.8$) positions the network's behavior to be maximally sensitive to the level of contralateral inhibition. At this neutral point, the stability of the antisymmetric subsystem can be pushed into instability by the smallest changes in I_C.

Model variants: one unit or multiple units on each side

The behaviors described above apply to model variants that have only one unit on each side, or more than two units, provided that they have the same connectivity pattern as the original model. The analysis is entirely parallel to the analysis detailed above, and we summarize it here.

We consider a model with N units on each side, each reciprocally connected to a single stop unit with inhibitory strength k_S, and each reciprocally connected to all units on the opposite side with inhibitory strength k_C. As in the original model, we postulate that summed signals from bilaterally-symmetric units control forward velocity, and differences control angular velocity.

The linearized model retains the form of eq. (6), and the connectivity pattern is embodied in a $(2N+1)\times(2N+1)$ matrix L given by

$$L=\begin{bmatrix} k_E & 0 & \cdots & 0 & -k_S & -k_C & \cdots & \cdots & -k_C \\ 0 & \ddots & \ddots & \vdots & \vdots & \vdots & & & \vdots \\ \vdots & \ddots & k_E & 0 & -k_S & -k_C & & & \vdots \\ 0 & \cdots & 0 & k_E & -k_S & -k_C & -k_C & \cdots & -k_C \\ -k_S & \cdots & -k_S & -k_S & k_E & -k_S & -k_S & \cdots & -k_S \\ -k_C & \cdots & -k_C & -k_C & -k_S & k_E & 0 & \cdots & 0 \\ \vdots & & & -k_C & -k_S & 0 & k_E & \ddots & \vdots \\ \vdots & & & \vdots & \vdots & \vdots & \ddots & \ddots & 0 \\ -k_C & \cdots & \cdots & -k_C & -k_S & 0 & \cdots & 0 & k_E \end{bmatrix}. \tag{28}$$

A rotation analogous to eq.(12) splits the system into a symmetric subsystem of dimension $N+1$ and an antisymmetric subsystem of dimension N (analogous to eqs. (17)), with

$$L_{sym}=\begin{bmatrix} k_E-k_C & -k_C & \cdots & -k_C & -k_S\sqrt{2} \\ -k_C & \ddots & \ddots & \vdots & \vdots \\ \vdots & \ddots & k_E-k_C & -k_C & -k_S\sqrt{2} \\ -k_C & \cdots & -k_C & k_E-k_C & -k_S\sqrt{2} \\ -k_S\sqrt{2} & \cdots & -k_S\sqrt{2} & -k_S\sqrt{2} & k_E \end{bmatrix},\ L_{anti}=\begin{bmatrix} k_E+k_C & k_C & \cdots & k_C \\ k_C & k_E+k_C & \ddots & \vdots \\ \vdots & \ddots & \ddots & k_C \\ k_C & \cdots & k_C & k_E+k_C \end{bmatrix}. \tag{29}$$

Via methods analogous to those used above, the symmetric subsystem is found to have $N-1$ eigenvalues equal to k_E, and two other eigenvalues given by

$$\lambda_{\pm}=k_E-\frac{Nk_C}{2}\pm\sqrt{\left(\frac{Nk_C}{2}\right)^2+2Nk_S{}^2}\,. \tag{30}$$

The antisymmetric subsystem has $N-1$ eigenvalues equal to k_E and one eigenvalue given by

$$\lambda_{E+NC}=k_E+Nk_C\,. \tag{31}$$

With $N=2$, eq. (30) corresponds to eq. (23) and eq. (31) corresponds to eq. (26).

Thus, the stability behavior of a model with N units on each side is identical to that of the original model. In particular, k_C but not k_S contributes to instability in the antisymmetric subsystem. In detail, a model with N units on each side effectively multiplies the contralateral inhibitory strength k_C by N, multiplies the stop strength k_S by $\sqrt{N}$, and creates $N-1$ eigenvalues equal to k_E in both subsystems.

Figure 1

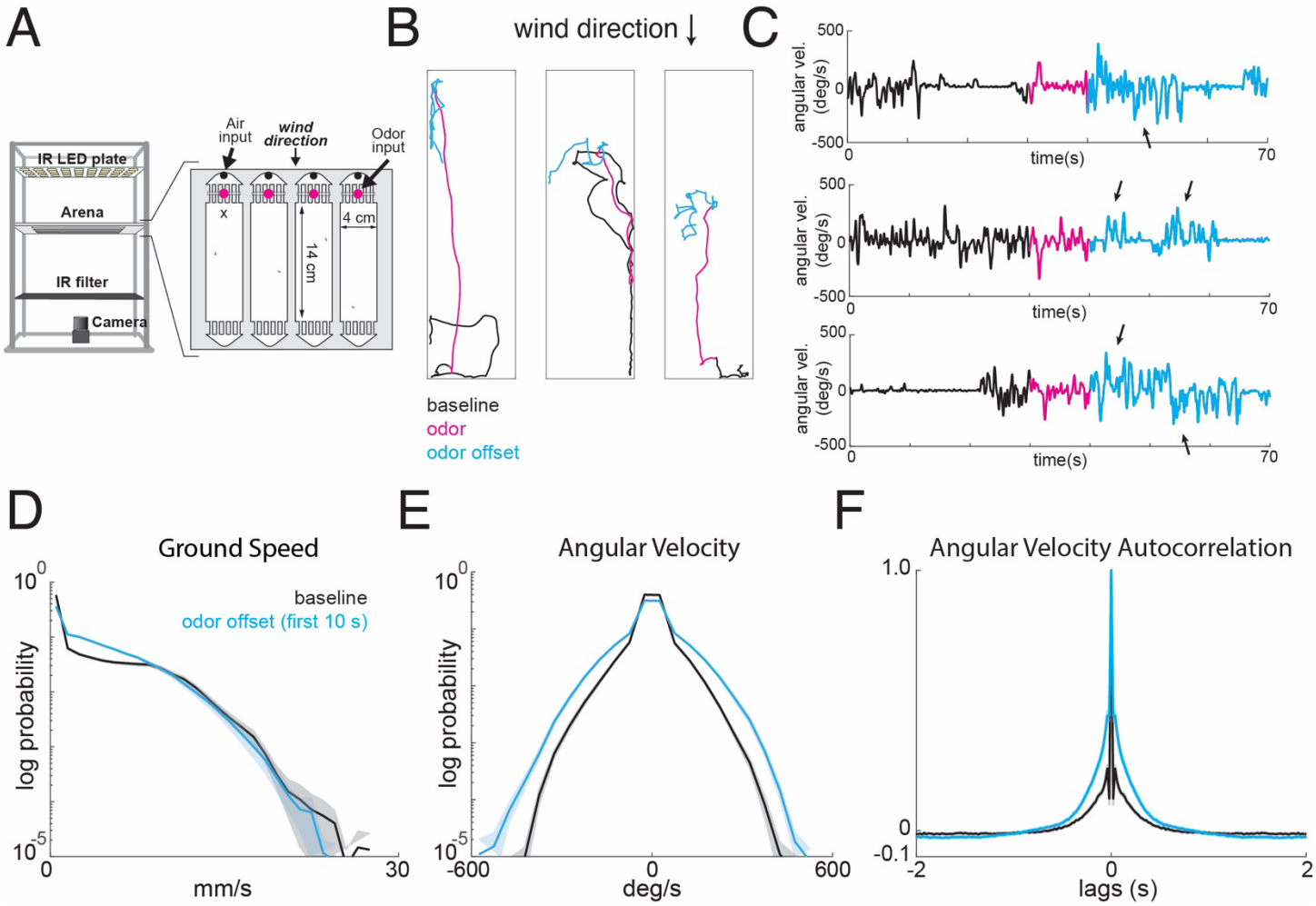

Fig 1. Odor loss drives systematic changes in locomotor statistics

A. Schematic of wind tunnel apparatus. Flies are constrained to walk in shallow 4 by 14 cm arenas and presented with temporally controlled wind and odor stimuli. Walking behavior is monitored using IR LEDs and a camera.

B. Example trajectories of walking flies presented with a 10 s odor pulse (10% apple cider vinegar) centered in 70 s of laminar wind (left). Black: pre-odor baseline; magenta: odor period; cyan: post-odor. Flies move upwind towards the wind source in response to odor and perform a local search following odor offset. Wind direction indicated by arrow.

C. Time course of angular velocity for examples shown in B. Note repeated turns in the same direction during post-odor period (cyan, arrows).

D. Distribution of ground speeds during the post-odor search phase (first 10 s after odor, cyan) versus pre-odor baseline walking (first 10 s of baseline, black). Lower ground speeds are favored during the post-odor period compared to baseline. Error bars represent standard error across flies (n=1306 total trajectories from 75 flies).

E. Distribution of angular velocities during the post-odor period (cyan) versus baseline walking (black). Larger angular velocities are favored during the post-odor period, compared baseline. Error bars represent standard error across flies. Same flies, trajectories, and time periods as in (D).

F. Autocorrelation of angular velocity during the post-odor period (cyan) versus baseline walking (black). Autocorrelogram widens during the post-odor period. Error bars represent standard error across flies. Same flies, trajectories, and time periods as in (D).

Figure S1

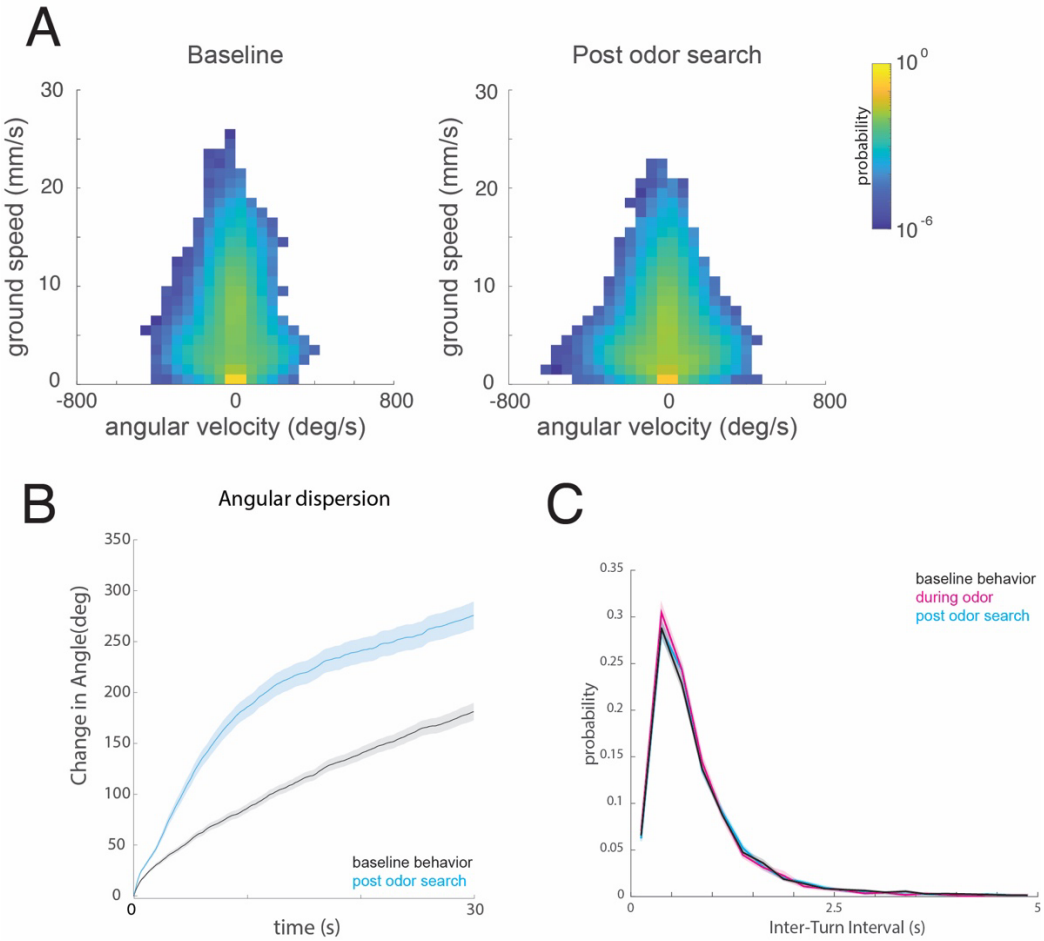

Supp Fig 1:

A. Two dimensional histograms of ground speed and angular velocity for the first 10 seconds of baseline behavior (left) and the first 10 seconds of post-odor search (right). Plots represent the mean histogram across flies (n=1306 total trajectories from 75 flies). Probability on the color axis. Same flies as in Fig 1D-F. Flies favor slower ground speeds and larger angular velocities after odor loss.

B. Angular dispersion as a function of time relative to heading at the start of trial (black, baseline period) or odor loss (cyan: post-odor period). Traces represent mean ± standard error across flies (n=1306 total trajectories from 75 flies). Same flies as in Fig 1D-F. Flies turn further after loss of odor when compared to baseline behavior.

C. Distribution of inter-turn intervals during baseline (black), odor (magenta), and post-odor periods (cyan) periods. Error bars represent standard error across flies (n=1306 total trajectories from 75 flies). Same flies as in Fig 1D-F.

Figure 2

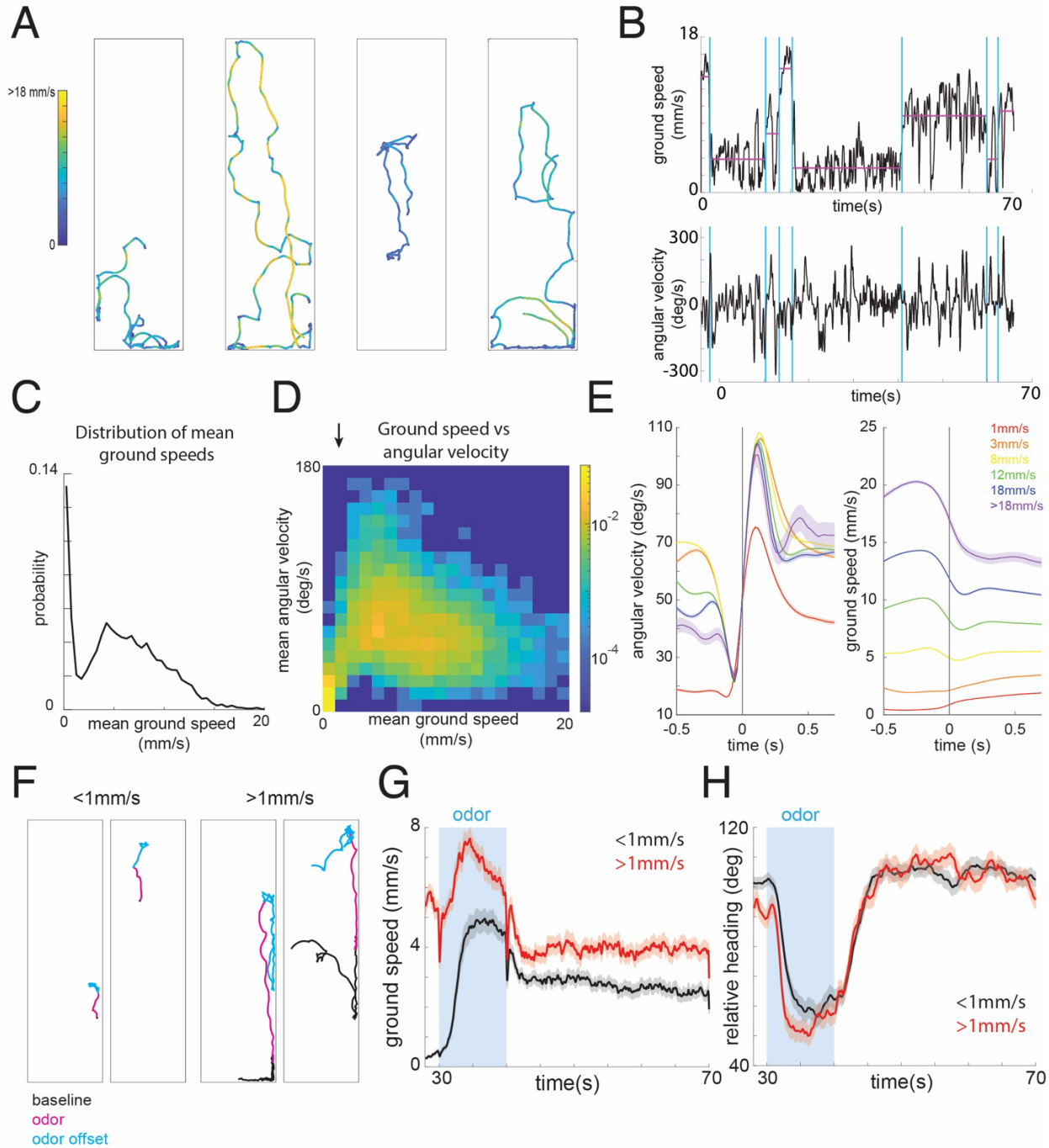

Fig 2. Spontaneous variation in locomotor states shapes responses to odor

A. Example trajectories illustrating spontaneous variation in locomotor statistics in the absence of odor. Colors indicate instantaneous ground speed as shown in color bar.

B. Time courses of ground speed and angular velocity for rightmost trajectory in (A), segmented into behavioral epochs using change point detection. Blue vertical lines indicate epochs and purple lines represent mean ground speed for each epoch.

C. Distribution of mean ground speeds during unstimulated walking for behavioral epochs segmented by change point detection, showing a bimodal distribution, corresponding to stationary and moving modes (n=898 trajectories from 56 flies).

D. Joint distribution of mean ground speed and mean angular velocity for all epochs segmented by change point detection. Angular velocity grows with ground speed between ~0-5 mm/s (black arrow), then decreases for higher ground speeds. Same flies as in (C).

E. Angular velocity (left) and ground speed (right) relative to turn onset. Turns were detected by threshold crossings in angular velocity, then sorted by ground speed in the 500 ms prior to turn onset. Curves represent means within each ground speed range (n=1306 trajectories from 75 flies, same flies as in Fig. 1D-F). Error bars represent standard error across turns within each category. At high ground speeds, we observe a decrease in ground speed preceding turn onset. At low ground speeds, acceleration follows turn onset.
F. Example trajectories of flies moving <1 mm/s at odor onset (left) and flies moving >1 mm/s at odor onset (right). Flies that were moving >1 mm/s at odor onset travel further in response to the odor stimulus.
G. Average ground speed for all trials where flies (N=75) were moving <1 mm/s at odor onset (black, 711 trials) and for trials where flies were moving >1 mm/s at odor onset (red, 595 trials). Trials where flies were moving >1 mm/s at odor onset show higher ground speeds during odor and after odor offset. Error bars represent standard error across fly means.
H. Average relative heading (upwind direction at 0 degrees) for all trials where flies were moving <1 mm/s at odor onset (black) and for trials where flies were moving >1 mm/s at odor onset (red). Trials where flies were moving >1 mm/s at odor onset show a more rapid orientation to the upwind direction. Error bars represent standard error across fly means.

Figure 3

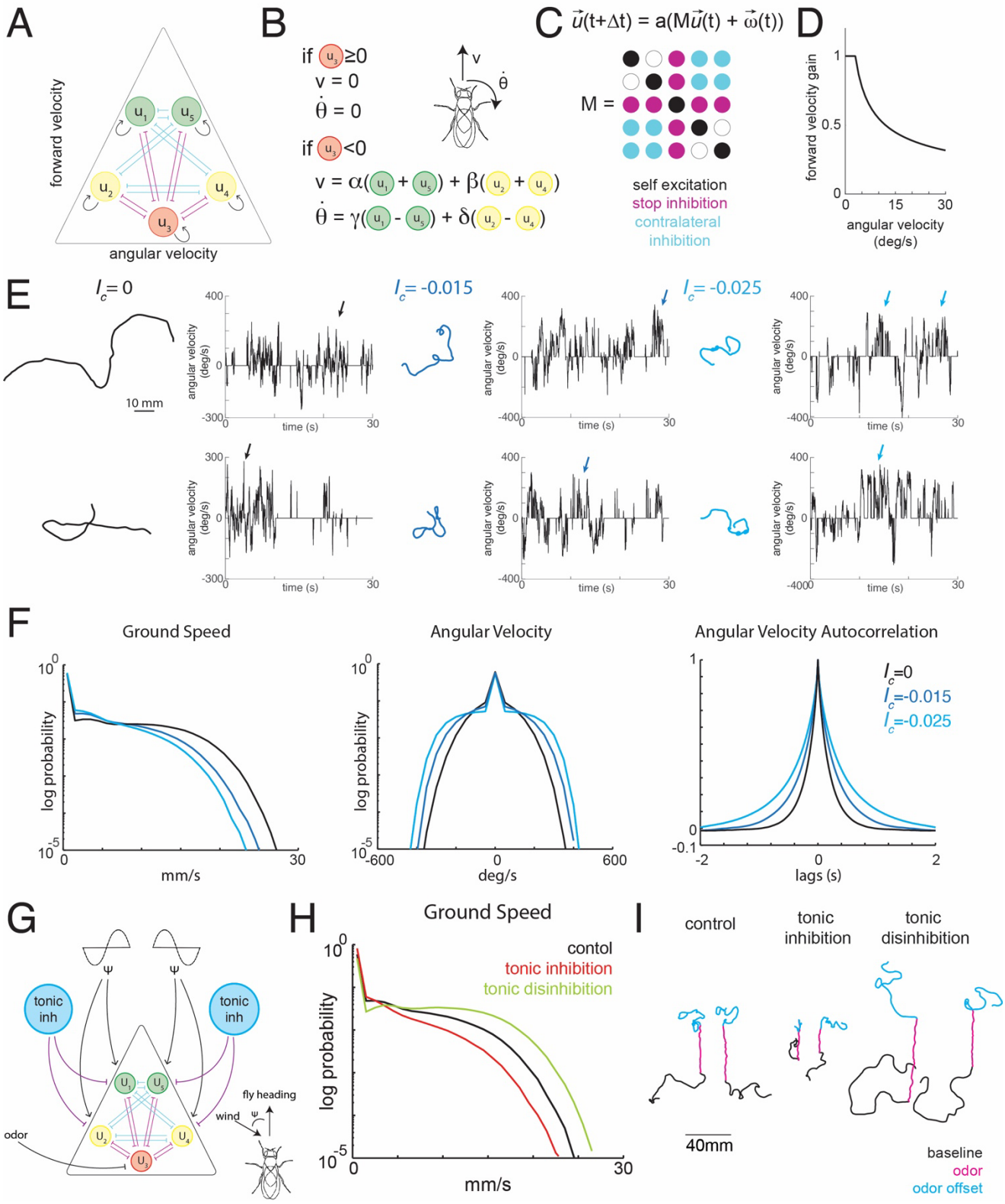

FIG 3: A physiologically inspired model can reproduce spontaneous and odor-evoked changes in locomotor statistics

A. Model locomotor control circuit comprised of five units. Green units (u_1 and u_5) drive large changes in forward velocity and small changes in angular velocity. Yellow units (u_2 and u_4) drive small changes in forward velocity and large changes in angular velocity. Red unit (u_3) drives stopping. All units excite themselves (black arrows) through a uniform positive weight. Movement-producing units (u_1, u_2, u_4, u_5)

and the stop unit (u_3) mutually inhibit each other through a uniform inhibitory weight (stop inhibition, magenta). Left (u_1 and u_2) and right ($u_4$and u_5) movement-producing units mutually inhibit each other through a second uniform inhibitory weight (contralateral inhibition, cyan).

B. Relationship between unit activity and locomotion. Positive activity in the stop unit ($u_3 \geq 0$) suppresses forward movement and turning. When activity in the stop unit is negative, forward velocity is calculated as a weighted sum of all movement-producing units and angular velocity is calculated as a sum of the weighted difference between paired units on either side of the model.

C. Unit dynamics are governed by a connectivity matrix M. Unit activity at time $t + \Delta t$ is computed by multiplying the activity at the previous time step t by the matrix M, adding independent Gaussian noise ($\vec{\omega}$) to each unit, and then applying a sigmoid nonlinearity a. See Methods for further details.

D. A gain function g (see Methods) reduces forward velocity when angular velocity is high, resulting in sharper large turns.

E. Example trajectories of model flies with different amounts of contralateral inhibition (I_c) and associated angular velocity traces. In the absence of contralateral inhibition (left), trajectories are relative straight and left and right turns are intermingled (black arrows). As contralateral inhibition increases, trajectories become more tortuous, and the model produces runs of turns in the same direction (blue and cyan arrows), similar to experimental trajectories observed during offset search.

F. Statistical features of locomotion in model flies (from 1300 model trajectories) as a function of the strength of contralateral inhibition. Left: Ground speed distribution, center: angular velocity distribution, right: autocorrelation of angular velocity. Increased contralateral inhibition shifts the ground speed distribution towards lower values, shifts the angular velocity distribution towards higher values, and widens the autocorrelogram of angular velocity, similar to what we observe during post-odor search (Fig. 1D-F).

G. Model schematic with the addition of odor- and wind-gated terms. To drive upwind running, odor suppresses the activity of the stop unit (u_3) and modulates activity in the movement-producing units (u_1, u_2, u_4, u_5) according to a steering function that depends on wind direction. To modulate overall locomotor speed, tonic feedforward inhibition acts uniformly on all movement-producing units.

H. Distribution of ground speeds produced by the model (from 500 model trajectories) with no feedforward inhibition (black), feedforward inhibition (red), and feedforward disinhibition (green). Tonic inhibition and disinhibition shift the distribution of ground speeds to lower or higher values respectively.

I. Example odor-evoked trajectories produced by the model in the absence of feedforward inhibition (left), with feedforward inhibition (middle), and with feedforward disinhibition (right). Black: baseline walking; magenta: odor; cyan: post-odor search. Feedforward inhibition shrinks resultant trajectories, while disinhibition lengthens trajectories, mimicking shifts seen across behavioral modes in experimental data.

Figure S2

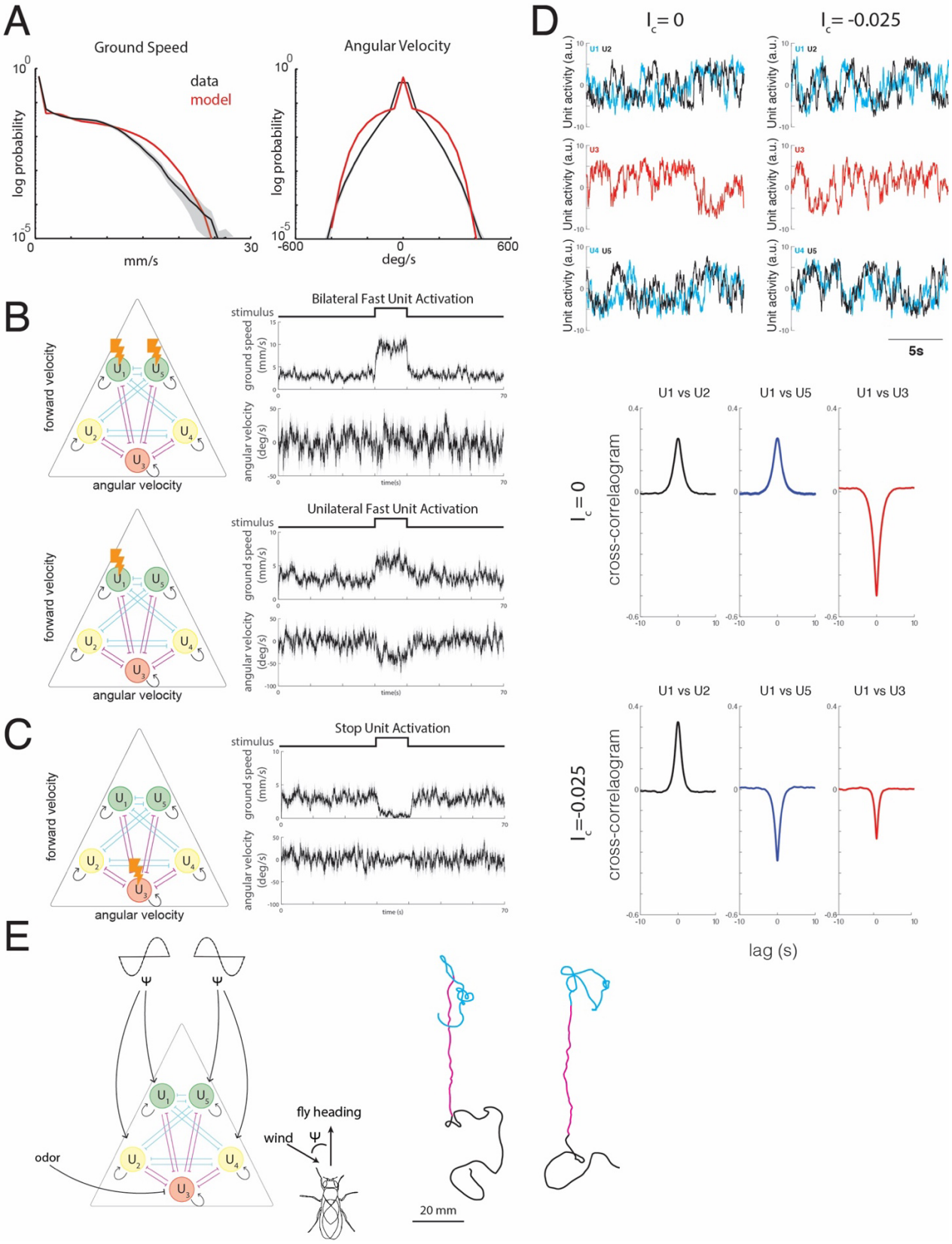

Supp Fig 2:

A. Distributions of ground speed (left) and angular velocity (right) produced by the model (red) after tuning the model coefficients ($\alpha,\beta,\gamma,\delta$), overlaid on experimental distributions (black) for baseline walking. Model data computed from 1300 generated trajectories. Baseline data reproduced from Fig.1D,E.

B. Effects of unit activation on locomotor parameters. Top: bilateral activation of u_1 and u_5 drives an increase in ground speed with no net change in angular velocity. Bottom: unilateral activation of u_1 drives turning, indicated here by a negative shift in angular velocity, and a smaller increase in ground speed.
C. Effects of stop unit activation on locomotor parameters. Activation of the stop unit u_3 drives an abrupt decrease in ground speed.
D. Unit activity in the absence (left) and presence (right) of contralateral inhibition (I_c). In the absence of contralateral inhibition activity in a locomotor unit (u_1) is correlated both with the unit on the same side (u_2) and on the opposite side (u_5) but is negatively correlated with activity in the stop unit (u_3)— quantified in middle plot below. In the presence of contralateral inhibition (right) activity in units on opposite sides becomes anti-correlated – quantified in bottom plot – resulting in larger angular velocities and smaller forward velocities.
E. Model schematic with the addition of odor- and wind-gated terms (left). Odor suppresses the activity of the stop-producing unit (u_3). Heading is compared to wind direction to generate upwind turn commands in movement-producing units (u_1, u_2, u_4, u_5). Resulting trajectories (right). Black: baseline walking, magenta: odor, cyan: post-odor search.

Figure S3

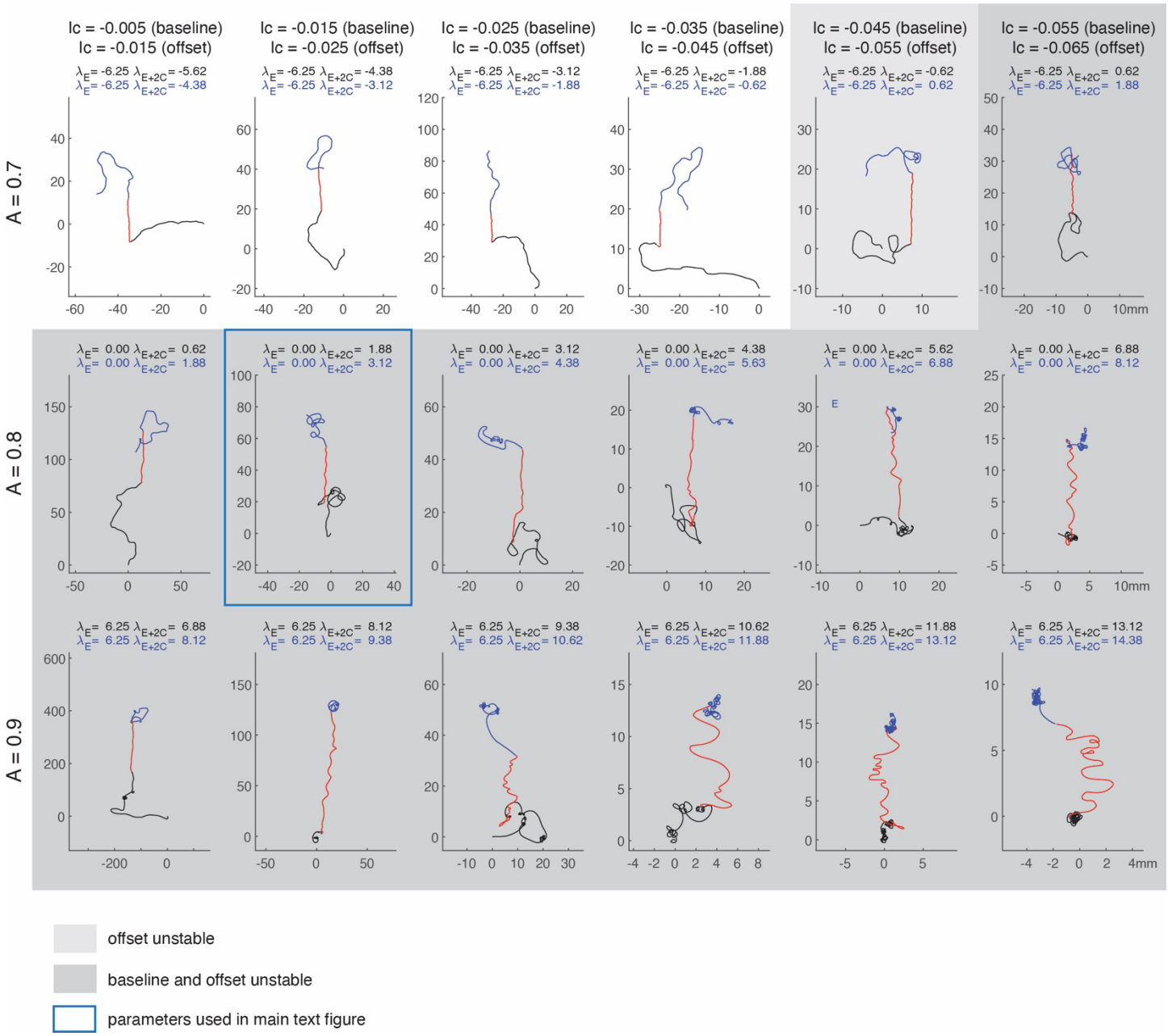

Supp Fig 3:
Trajectories produced by the model in the main text, as the self-excitation parameter A is varied (top to bottom: 0.7, 0.8, 0.9) and the contralateral inhibition parameter I_c is varied (left to right: -0.005 to -0.055 in steps of -0.01). As in the main text, $I_s = -0.03$, I_c is made more negative by 0.01 after odor offset, and the odor is off for 30 sec (black), then on for 10 sec (red), then off 30 sec (blue). Other model parameters are unchanged. A gray background indicates that one or both phases of the trajectory have an unstable anti-symmetric component, as shown in the legend. The second panel in the second row corresponds to the model parameters in the main text (blue rectangle). Numbers in each panel indicate the eigenvalues for the fixed point of the antisymmetric component for baseline (black) and odor-offset (blue) parameters. Note the change in overall trajectory size, as indicated by the scale bars.

Figure 4

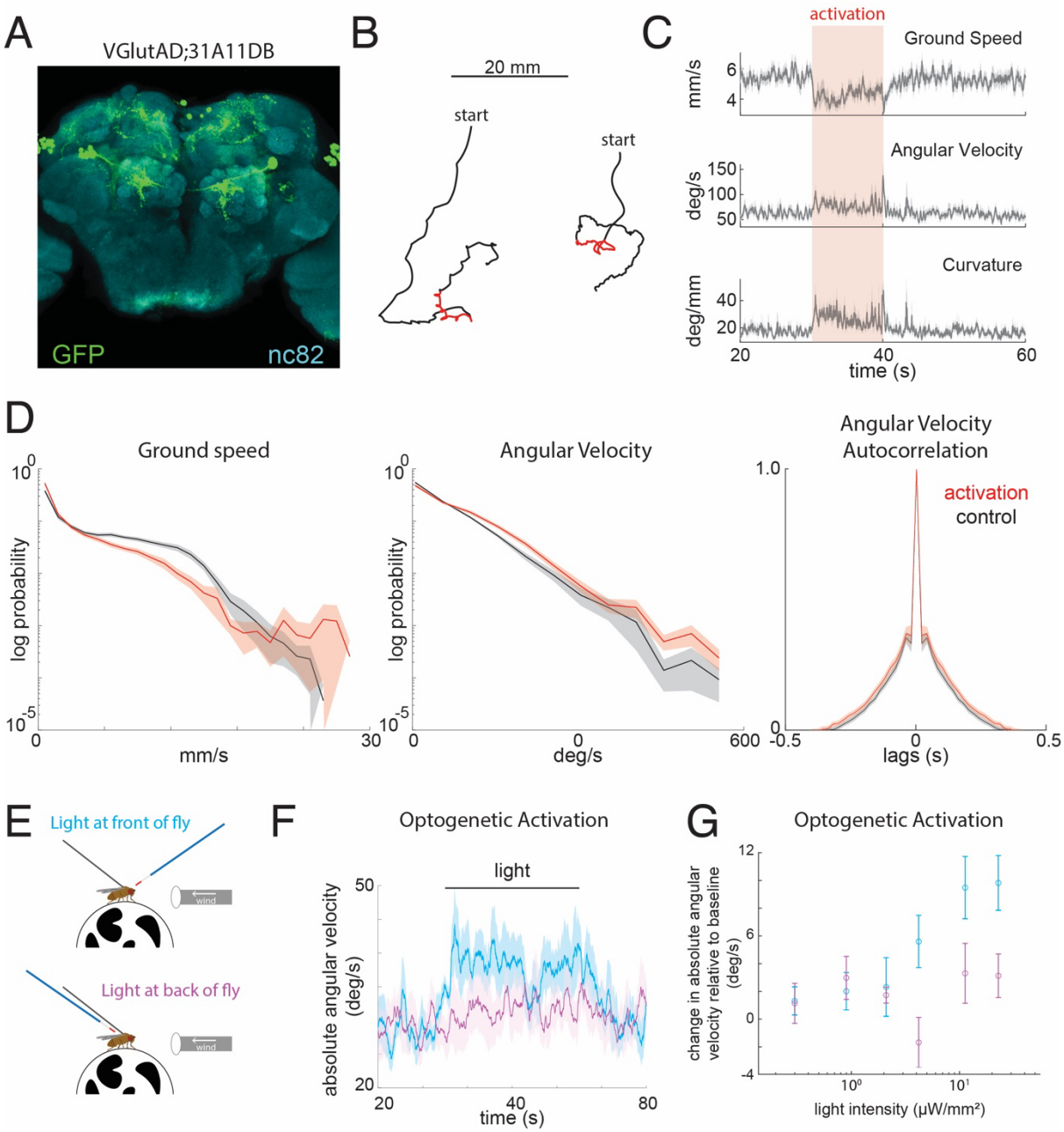

FIG 4: A population of inhibitory neurons regulates curvature

F. Confocal image of neurons labeled by VGlut-AD;31A11-DBD > GFP (green). Neuropil (nc82) in cyan. This line labels 5-6 neurons in each LAL that project contralaterally to the opposite LAL, as well as small populations of neurons in SIP and LH and in the VNC (see Supp. Fig 4C).

G. Example trajectories in which VGlut-AD;31A11-DBD neurons were activated with Chrimson. Black: no light; red: light.

H. Average time course of ground speed, angular velocity, and curvature response to Chrimson activation in VGlut-AD;31A11-DBD neurons (red: 10s). Error bars represent standard error across fly means. (n=183 total trials from 31 flies). Activation causes a decrease in ground speed, an increase in angular velocity, and an increase in curvature.

I. Distributions of ground speed (left), absolute value of angular velocity (middle), and autocorrelation of angular velocity (right) in VGlut-AD;31A11-DBD>Chrimson flies in the presence (red) and absence (black) of light. Error bars represent standard error across flies (n=183 total trials from 31 flies). Activation shifts

ground speed towards lower values and shifts angular velocity towards higher values, similar to post-odor search (Fig. 1C-E). For this plot, data during non-moving periods (ground speed <1 mm/s) were excluded. Equivalent plot for the effect of odor offset on angular velocity is shown in Supp Fig. 4D.

J. Schematic of walking ball experiments to distinguish effects of brain and VNC neurons on behavior. A tethered fly walks on an air-supported ball in the presence of frontal wind at 10cm/s. Two fiber optic cables are aimed at the head (front) and thorax (back) and deliver red light of varying intensities.

K. Effects of frontal (cyan) and rear (magenta) light presentation at 11.3 $\mu W/mm^2$ on the angular velocity of VGlut-AD;31A11-DBD > Chrimson flies. Mean behavioral response to 5 light pulses was calculated for each fly. Traces represent mean ± standard error across flies (n=8 flies). Frontal stimulation elicited stronger behavior, arguing that behavioral effects arise from brain rather than VNC neurons.

L. Change in absolute angular velocity (mean ± standard error) as a function of light level for frontal (cyan) and rear (magenta) light presentation. Graded changes in light from the front produce graded changes in locomotor behavior.

Figure S4

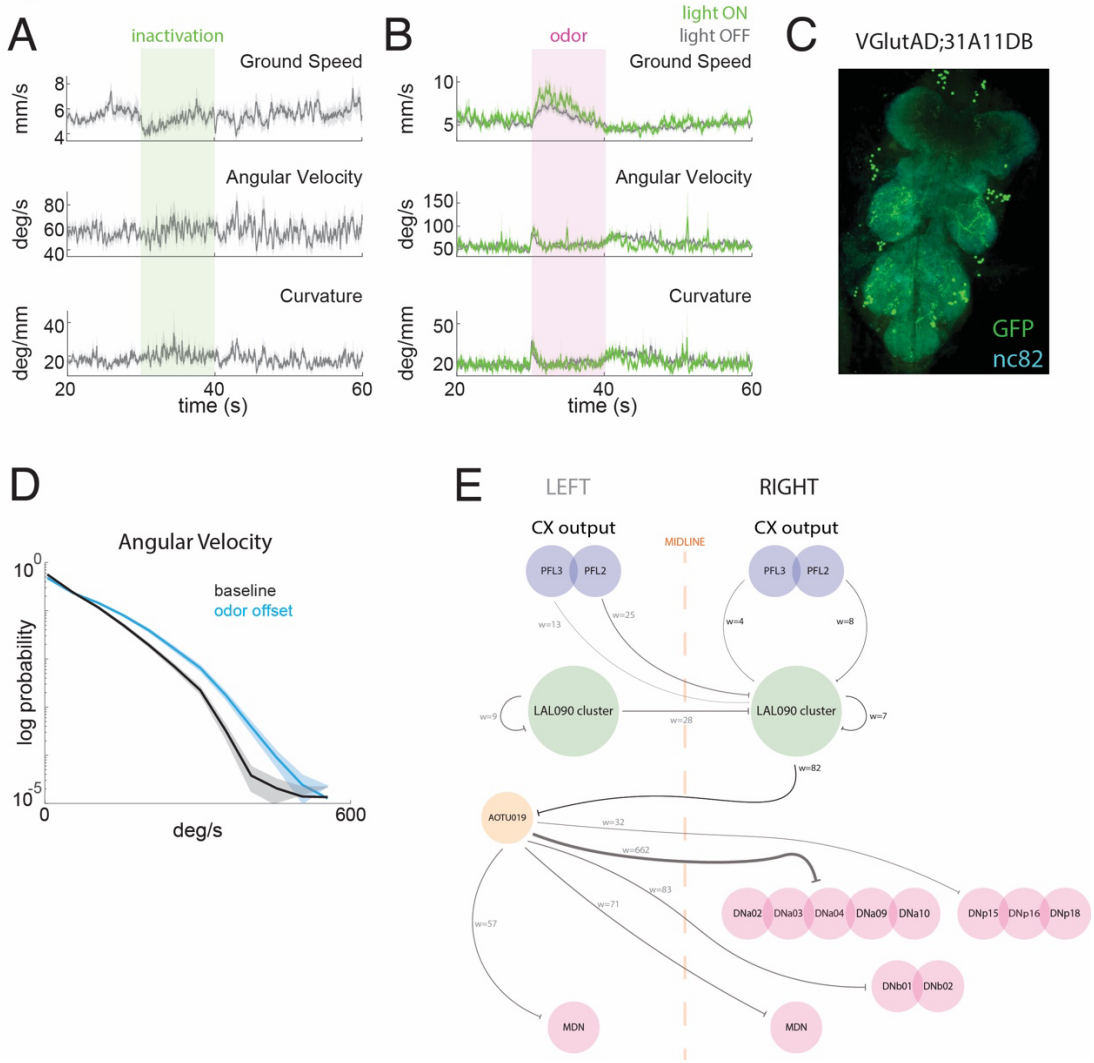

Supp Fig 4:

A. Average time course of ground speed, angular velocity, and curvature in response to optogenetic silencing of VGlut-AD;31A11-DBD neurons with GtACR (green: 10s, 1.082mW/cm^2). Traces represent mean ± standard error across flies (n=199 total trials from 23 flies). Inactivation had minimal effects on locomotor parameters.

B. Effects of VGlut-AD;31A11-DBD>GtACR inactivation on odor responses. Average time course of ground speed, angular velocity, and curvature in response to 10 s of odor (magenta, 1% ACV) in VGlut-AD;31A11-DBD>GtACR flies in the presence (green, n= 180 total trials from 21 flies, 1.082mW/cm^2) and absence (black, n=326 total trials from 24 flies) of green light. Traces represent mean ± standard across flies. Inactivation slightly increases ground speed during odor but does not substantially reduce the curvature response at odor offset.

C. Confocal image of neurons in the ventral nerve cord (cyan) labeled by VGlut-AD;31A11-DBD>GFP (green). Neuropil (nc82) in cyan.

D. Distribution of absolute value of angular velocity during baseline walking (black) and post odor search (cyan) in control flies with non-moving periods (ground speed <1mm/s) excluded. Error bars represent standard error across flies (n=1306 total trajectories from 75 flies). Same flies and trials as in Fig1E.

E. Connectomic analysis of VGlut-AD;31A11-DBD neurons. These neurons form both input and output arbors in the medial LAL without notable projections outside of this zone. We believe this line most likely labels neurons LAL091-095 in the hemibrain connectome. This population receives strong bilateral innervation from PFL2 neurons in the Central Complex and makes indirect outputs to DNs though the neuron AOTU019.

Figure 5

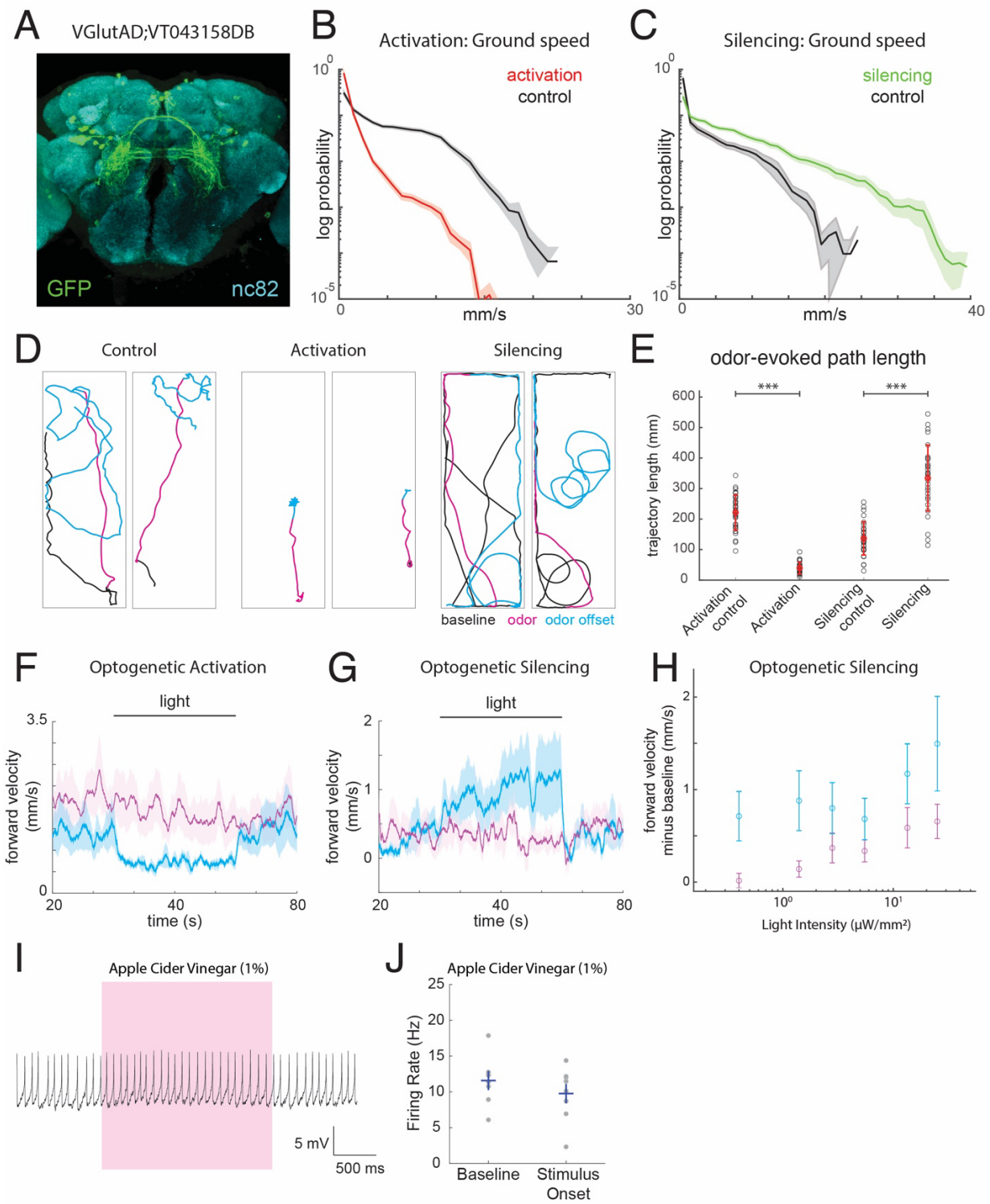

FIG 5: A population of inhibitory neurons bi-directionally regulates ground speed

A. Confocal image of neurons labeled by VGlut-AD;VT043158-DBD > GFP (green). Neuropil (nc82) in cyan. This line labels ~10 neurons in each LAL that project contralaterally to the opposite LAL, 2 bilateral pairs of neurons along the dorsal midline, as well as neurons in the VNC (Supp. Fig. 4A).

B. Distribution of ground speeds of VGlut-AD;VT043158-DBD > Chrimson flies in the presence of light (red) and absence of light (black). Traces represent mean ± standard error across flies (n=337 total trials from 34 flies). Activation shifts ground speed to lower values.

C. Distribution of ground speeds of VGlut-AD;VT043158-DBD > GtACR1 flies in the presence of light (green) and absence of light (black). Traces represent mean ± standard error across flies (n=219 total trials from 23 flies). Silencing shifts ground speed to higher values.
D. Example trajectories in response to an odor pulse (10s of 1% ACV) in the absence of light (Chrimson control, left), during optogenetic activation of VGlut-AD;VT043158-DBD neurons with Chrimson (middle), and during optogenetic silencing of VGlut-AD;VT043158-DBD neurons with GtACR1 (right).
E. Path length of odor-evoked runs under different stimulation conditions. Each black dot represents mean of trials for one fly. Red symbols indicate mean ± standard deviation across flies. Activation of VGlut-AD;VT043158-DBD neurons significantly reduces path length (unpaired t-test: $p=2.8756x10^{-23}$, n=469 trials total from 34 flies for control and 192 total trials from 28 flies for activation) while silencing significantly increase path length ($p= 2.1377X10^{-12}$, n=280 total trials from 30 flies for control and 229 total trials from 29 flies for silencing).
F. Effects of frontal (cyan) and rear (magenta) light presentation at 0.3 $\mu W/mm^2$ on the ground speed of VGlut-AD;VT043158-DBD > Chrimson flies. Mean behavioral response to 5 light pulses was calculated for each fly. Traces represent mean ± standard error across fly means (n=8 flies). Frontal stimulation elicited stronger behavior, arguing that behavioral effects arise from brain rather than VNC neurons.
G. Effects of frontal (cyan) and rear (magenta) light presentation at 0.4 $\mu W/mm^2$ on the ground speed of VGlut-AD;VT043158-DBD > GtACR1 flies. Mean behavioral response to 5 light pulses was calculated for each fly. Traces represent mean ± standard error across fly means (n=8 flies). Frontal stimulation again elicited stronger behavior.
M. Change in ground speed (mean ± standard error) as a function of light level during frontal (cyan) and rear (magenta) GtACR1-mediated silencing.
N. Example recording of a LAL neuron labeled by VGlut-AD;VT043158-DBD > GFP. Note tonic activity.
O. Mean firing rate of LAL neurons labeled by VGlut-AD;VT043158-DBD > GFP during baseline and 1% ACV. Gray symbols represent mean for each cell; blue crosses represent mean across cells (n = 8 cells).

Figure 6

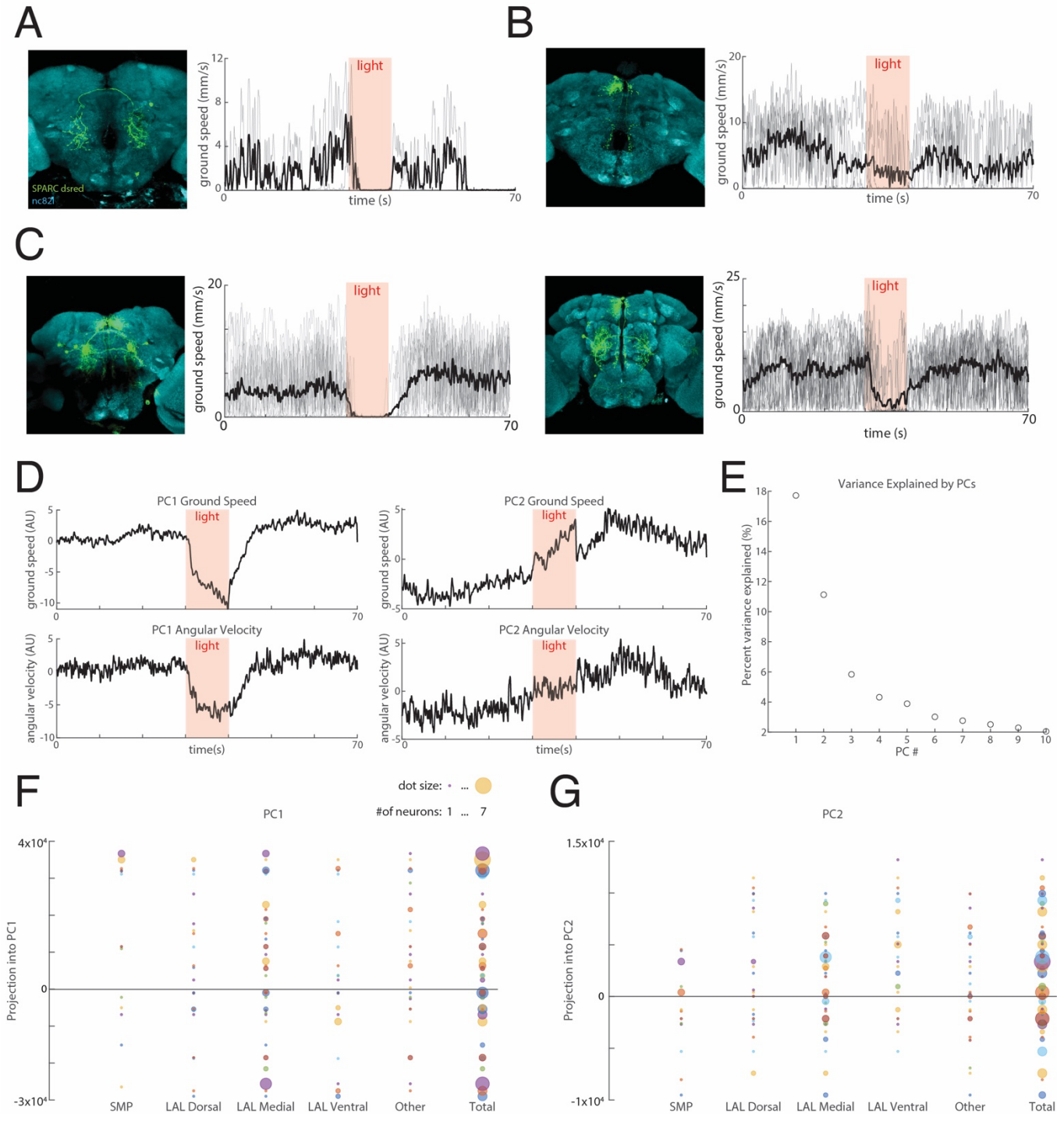

FIG 6: Sparse activation suggests that both LAL and SMP neurons contribute to speed control

A. Confocal image of a single neuron clone obtained from sparse labelling of VGlut-AD;VT043158-DBD with SPARC2-S-CsChrimson-tdTomato (tdTomato: green, neuropil: cyan) and associated ground speed in response to Chrimson activation (trials in grey, mean in black, light: 14.6μW/mm^2). This neuron was classified as a “LAL dorsal” neuron. Activation resulted in stopping.

B. Confocal image of a single neuron clone obtained from sparse labelling of VGlut-AD;VT043158-DBD with SPARC2-I-CsChrimson-tdTomato (tdTomato: green, neuropil: cyan) and associated ground speed in response to Chrimson activation (trials in grey, mean in black, light: 14.6μW/mm^2). This neuron was classified as an “SMP” neuron. Activation resulted in weak slowing.

C. Confocal images of brains with multiple neurons labeled by VGlut-AD;VT043158-DBD > SPARC2-I-CsChrimson-tdTomato (tdTomato: green, neuropil: cyan) and associated ground speed responses as in A. Both LAL and SMP neurons are labeled. Activation of these populations caused robust slowing or stopping.
D. Principal components of the behavioral response to optogenetic activation across all VGlut-AD;VT043158-DBD > SPARC Chrimson flies (n=53 flies). The first principal component (left) consists of a rapid decrease in both ground speed and angular velocity. The second principal component (right) consists of a slower and more persistent increase in both ground speed and angular velocity.
E. Scree plot of percent variance explained by each of the first 10 principal components.
F. Projection onto PC1 as a function of anatomical labeling in each fly. Position along the y-axis represents the projection of mean fly ground speed and angular velocity onto the first principal component. Marker size indicates the number of neurons that fall into each anatomical class for each brain. A total count of all neurons of interest (excluding neurons classified as ‘other’) in the rightmost column. Note larger numbers of SMP neurons labeled in flies with strong projections on PC1.
G. Same as F for PC2.

Figure S5

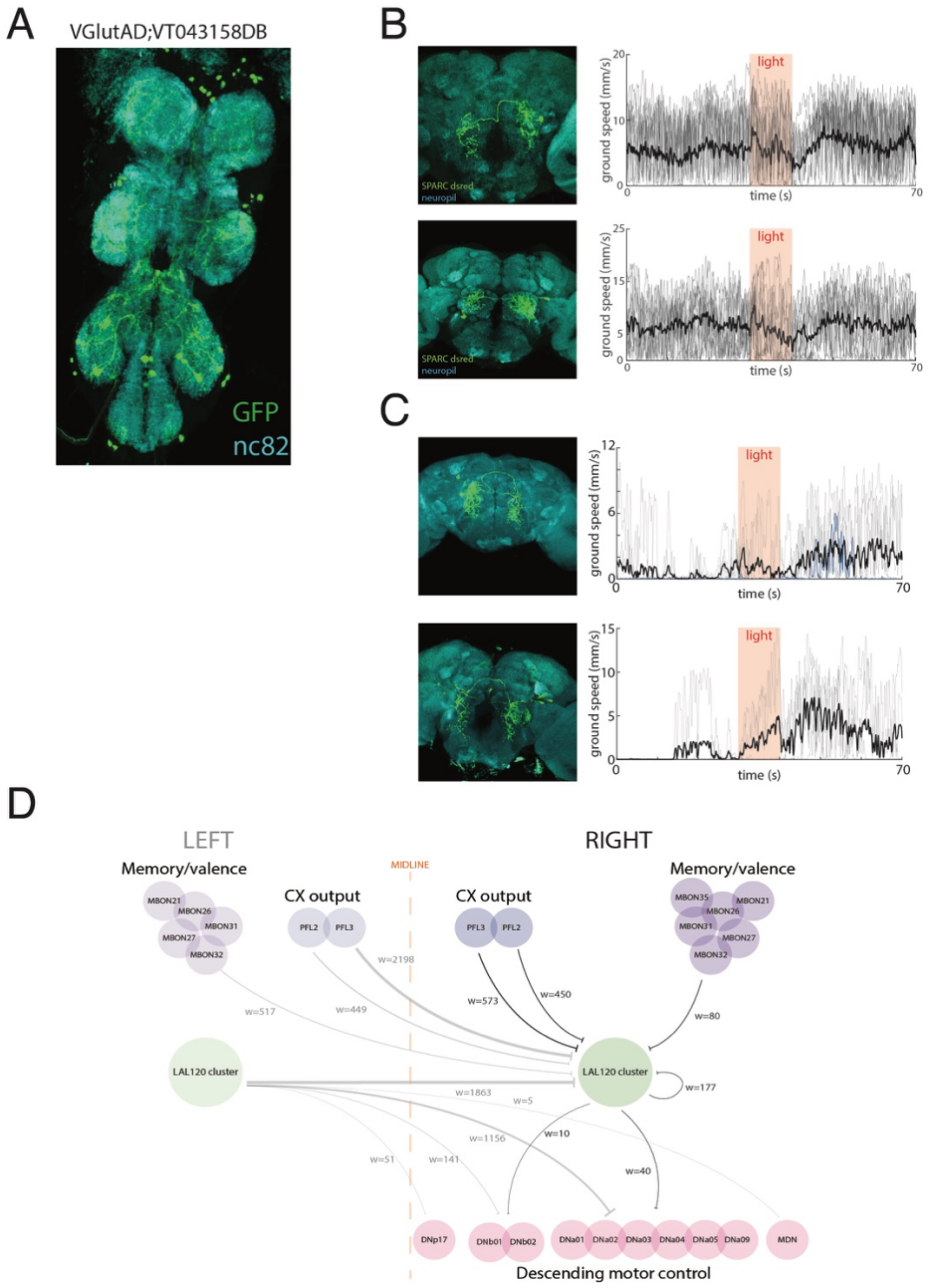

Supp Fig 5:

A. Confocal image of VGlut-AD;VT043158-DBD neurons labeled in the ventral nerve cord (green). Neuropil in cyan.

B. Confocal image of additional single neuron clones obtained from sparse labelling of VGlut-AD;VT043158-DBD>SPARC-Chrimson (tdtomato: green, neuropil: cyan) and associated ground speed responses (trials in grey, mean in black, light: 0.576mW/cm2). One neuron labelled as “LAL ventral” (top) and one labelled as “LAL medial” (bottom) both drive small transient increases in ground speed followed by weak slowing.

C. Examples of sparsely labeled brains that drive behavior with strong projections onto PC2. Colors and symbols as in A. Activation of both caused a slow increase in ground speed.

D. Connectomics analysis of LAL neurons labeled by VGlut-AD;VT043158-DBD. This population has large anterior cell bodies and sends projections across the midline in two commissures. We believe this line most likely labels neurons LAL073-074 and LAL120-126 in the hemibrain connectome. This population receives strong contralateral and weaker ipsilateral input from PFL2 and PFL3 neurons and a select group of MBONs. This population has strong contralateral projections to many DNs, including DNa01, a02, a03, a04, a05, a09, b01, b02, p17, and MDN.

References

Adden, A., Stewart, T. C., Webb, B., & Heinze, S. (2022). A neural model for insect steering applied to olfaction and path integration. *Neural computation*, *34*(11), 2205-2231.

Álvarez-Salvado, E., Licata, A. M., Connor, E. G., McHugh, M. K., King, B. M., Stavropoulos, N., Victor, J. D., Crimaldi, J. P., & Nagel, K. I. (2018). Elementary sensory-motor transformations underlying olfactory navigation in walking fruit-flies. *eLife*, *7*, e37815. https://doi.org/10.7554/eLife.37815

Aymanns, F., Chen, C. L., & Ramdya, P. (2022). Descending neuron population dynamics during odor-evoked and spontaneous limb-dependent behaviors. *eLife*, *11*, e81527. https://doi.org/10.7554/eLife.81527

Banks, C. J. (1957). The behaviour of individual coccinellid larvae on plants. *The British Journal of Animal Behaviour*, *5*(1), 12-24.

Ben Arous, J., Laffont, S., & Chatenay, D. (2009). Molecular and sensory basis of a food related two-state behavior in C. elegans. *PloS one*, *4*(10), e7584. https://doi.org/10.1371/journal.pone.0007584

Berman, G. J., Bialek, W., & Shaevitz, J. W. (2016). Predictability and hierarchy in Drosophila behavior. *PNAS*, *113*(42), 11943–11948. https://doi.org/10.1073/pnas.1607601113

Bidaye, S. S., Laturney, M., Chang, A. K., Liu, Y., Bockemühl, T., Büschges, A., & Scott, K. (2020). Two Brain Pathways Initiate Distinct Forward Walking Programs in Drosophila. *Neuron*, *108*(3), 469–485.e8. https://doi.org/10.1016/j.neuron.2020.07.032

Braun, J., Hurtak, F., Wang-Chen, S., & Ramdya, P. (2023). Networks of descending neurons transform command-like signals into population-based behavioral control. *bioRxiv*, 2023.09.11.557103. https://doi.org/10.1101/2023.09.11.557103

Brezovec, L. E., Berger, A. B., Druckmann, S., & Clandinin, T. R. (2023). Neural correlates of future volitional action in Drosophila. *bioRxiv*, 2023-09.

Brezovec, B. E., Berger, A. B., Hao, Y. A., Chen, F., Druckmann, S., & Clandinin, T. R. (2022). Mapping the neural dynamics of locomotion across the drosophila brain. *Current Biology*.

Calhoun, A. J., Pillow, J. W., & Murthy, M. (2019). Unsupervised identification of the internal states that shape natural behavior. *Nature neuroscience*, *22*(12), 2040–2049. https://doi.org/10.1038/s41593-019-0533-x

Cande, J., Namiki, S., Qiu, J., Korff, W., Card, G. M., Shaevitz, J. W., ... & Berman, G. J. (2018). Optogenetic dissection of descending behavioral control in Drosophila. *Elife*, *7*, e34275.

Carreira-Rosario, A., Zarin, A. A., Clark, M. Q., Manning, L., Fetter, R. D., Cardona, A., & Doe, C. Q. (2018). MDN brain descending neurons coordinately activate backward and inhibit forward locomotion. *eLife*, *7*, e38554. https://doi.org/10.7554/eLife.38554

Chandler, A. E. F. (1969). Locomotory behaviour of first instar larvae of aphidophagous Syrphidae (Diptera) after contact with aphids. *Animal Behaviour*, *17*(4), 673-678.

Cheong, H. S., Eichler, K., Stuerner, T., Asinof, S. K., Champion, A. S., Marin, E. C., ... & Card, G. M. (2023). Transforming descending input into behavior: The organization of premotor circuits in the Drosophila Male Adult Nerve Cord connectome. *bioRxiv*, 2023-06.

Cregg, J. M., Leiras, R., Montalant, A., Wanken, P., Wickersham, I. R., & Kiehn, O. (2020). Brainstem neurons that command mammalian locomotor asymmetries. *Nature Neuroscience*, *23*(6), 730–740. https://doi.org/10.1038/s41593-020-0633-7

Davies, A., Louis, M., & Webb, B. (2015). A Model of Drosophila Larva Chemotaxis. *PLoS computational biology*, *11*(11), e1004606. https://doi.org/10.1371/journal.pcbi.1004606

DeAngelis, B. D., Zavatone-Veth, J. A., & Clark, D. A. (2019). The manifold structure of limb coordination in walking *Drosophila*. *eLife*, *8*, e46409. https://doi.org/10.7554/eLife.46409

Demir, M., Kadakia, N., Anderson, H. D., Clark, D. A., & Emonet, T. (2020). Walking *Drosophila* navigate complex plumes using stochastic decisions biased by the timing of odor encounters. *eLife*, *9*, e57524. https://doi.org/10.7554/eLife.57524

Dorfman, A., Hills, T. T., & Scharf, I. (2022). A guide to area-restricted search: a foundational foraging behaviour. *Biological reviews of the Cambridge Philosophical Society*, *97*(6), 2076–2089. https://doi.org/10.1111/brv.12883

Eckstein, N., Bates, A. S., Champion, A., Du, M., Yin, Y., Schlegel, P., ... & Funke, J. (2020). Neurotransmitter Classification from Electron Microscopy Images at Synaptic Sites in Drosophila Melanogaster. *BioRxiv*, 2020-06.

Fleschner, C. (1950). Studies on searching capacity of the larvae of three predators of the citrus red mite. *Hilgardia*, *20*(13), 233-265.

Gomez-Marin, A., Stephens, G. J., & Louis, M. (2011). Active sampling and decision making in Drosophila chemotaxis. *Nature communications*, *2*, 441. https://doi.org/10.1038/ncomms1455

Guo, C., Pan, Y., & Gong, Z. (2019). Recent Advances in the Genetic Dissection of Neural Circuits in Drosophila. *Neuroscience bulletin*, *35*(6), 1058–1072. https://doi.org/10.1007/s12264-019-00390-9

Hsu, C. T., & Bhandawat, V. (2016). Organization of descending neurons in Drosophila melanogaster. *Scientific reports*, *6*, 20259. https://doi.org/10.1038/srep20259

Huang, K. H., Ahrens, M. B., Dunn, T. W., & Engert, F. (2013). Spinal projection neurons control turning behaviors in zebrafish. *Current Biology : CB*, *23*(16), 1566–1573. https://doi.org/10.1016/j.cub.2013.06.044

Hulse, B. K., Haberkern, H., Franconville, R., Turner-Evans, D., Takemura, S. Y., Wolff, T., Noorman, M., Dreher, M., Dan, C., Parekh, R., Hermundstad, A. M., Rubin, G. M., & Jayaraman, V. (2021). A connectome of the *Drosophila* central complex reveals network motifs suitable for flexible navigation and context-dependent action selection. *eLife*, *10*, e66039.

Isaacman-Beck, J., Paik, K. C., Wienecke, C. F. R., Yang, H. H., Fisher, Y. E., Wang, I. E., Ishida, I. G., Maimon, G., Wilson, R. I., & Clandinin, T. R. (2020). SPARC enables genetic manipulation of precise proportions of cells. *Nature Neuroscience*, *23*(9), 1168–1175. https://doi.org/10.1038/s41593-020-0668-9

Jayaram, V., Sehdev, A., Kadakia, N., Brown, E. A., & Emonet, T. (2023). Temporal novelty detection and multiple timescale integration drive Drosophila orientation dynamics in temporally diverse olfactory environments. *PLoS computational biology*, *19*(5), e1010606. https://doi.org/10.1371/journal.pcbi.1010606

Kanzaki, R., & Mishima, T. (1996). Pheromone-triggered 'Fiipflopping' neural signals correlate with activities of neck motor neurons of a male moth, Bombyx mori. *Zoological science*, *13*(1), 79-87.

Kashin, S. M., Feldman, A. G., & Orlovsky, G. N. (1974). Locomotion of fish evoked by electrical stimulation of the brain. *Brain research*, *82*(1), 41–47. https://doi.org/10.1016/0006-8993(74)90891-9

Katsov, A. Y., Freifeld, L., Horowitz, M., Kuehn, S., & Clandinin, T. R. (2017). Dynamic structure of locomotor behavior in walking fruit flies. *eLife*, *6*, e26410. https://doi.org/10.7554/eLife.26410

Kim, I. S., & Dickinson, M. H. (2017). Idiothetic Path Integration in the Fruit Fly Drosophila melanogaster. *Current Biology : CB*, *27*(15), 2227–2238.e3. https://doi.org/10.1016/j.cub.2017.06.026

Kimura, Y., Okamura, Y., & Higashijima, S. (2006). alx, a zebrafish homolog of Chx10, marks ipsilateral descending excitatory interneurons that participate in the regulation of spinal locomotor circuits. *The Journal of Neuroscience*, *26*(21), 5684–5697. https://doi.org/10.1523/JNEUROSCI.4993-05.2006

Lee, K., & Doe, C. Q. (2021). A locomotor neural circuit persists and functions similarly in larvae and adult *Drosophila*. *eLife*, *10*, e69767. https://doi.org/10.7554/eLife.69767

Leitch, K. J., Ponce, F. V., Dickson, W. B., van Breugel, F., & Dickinson, M. H. (2021). The long-distance flight behavior of *Drosophila* supports an agent-based model for wind-assisted dispersal in insects. *PNAS*, *118*(17), e2013342118. https://doi.org/10.1073/pnas.2013342118

Liu, W. W., & Wilson, R. I. (2013). Glutamate is an inhibitory neurotransmitter in the Drosophila olfactory system. *PNAS*, *110*(25), 10294-10299.

López-Cruz, A., Sordillo, A., Pokala, N., Liu, Q., McGrath, P. T., & Bargmann, C. I. (2019). Parallel Multimodal Circuits Control an Innate Foraging Behavior. *Neuron*, *102*(2), 407–419.e8. https://doi.org/10.1016/j.neuron.2019.01.053

Matheson, A. M. M., Lanz, A. J., Medina, A. M., Licata, A. M., Currier, T. A., Syed, M. H., & Nagel, K. I. (2022). A neural circuit for wind-guided olfactory navigation. *Nature communications*, *13*(1), 4613. https://doi.org/10.1038/s41467-022-32247-7

Murdie, G., & Hassell, M. P. (1973). Food distribution, searching success and predator-prey models. *The mathematical theory of the dynamics of biological populations*, 87-101.

Mussells Pires, P., Zhang, L., Parache, V., Abbott, L. F., & Maimon, G. (2024). Converting an allocentric goal into an egocentric steering signal. *Nature*, 10.1038/s41586-023-07006-3. Advance online publication. https://doi.org/10.1038/s41586-023-07006-3

Namiki, S., Dickinson, M. H., Wong, A. M., Korff, W., & Card, G. M. (2018). The functional organization of descending sensory-motor pathways in *Drosophila*. *eLife*, *7*, e34272. https://doi.org/10.7554/eLife.34272

Namiki, S., & Kanzaki, R. (2016). Comparative Neuroanatomy of the Lateral Accessory Lobe in the Insect Brain. *Frontiers in physiology*, *7*, 244. https://doi.org/10.3389/fphys.2016.00244

Okada, R., Sakura, M., & Mizunami, M. (2003). Distribution of dendrites of descending neurons and its implications for the basic organization of the cockroach brain. *Journal of Comparative Neurology*, *458*(2), 158-174.

Orger, M. B., Kampff, A. R., Severi, K. E., Bollmann, J. H., & Engert, F. (2008). Control of visually guided behavior by distinct populations of spinal projection neurons. *Nature neuroscience*, *11*(3), 327-333.

Paiva, V. H., Geraldes, P., Ramírez, I., Meirinho, A., Garthe, S., & Ramos, J. A. (2010). Foraging plasticity in a pelagic seabird species along a marine productivity gradient. *Marine Ecology Progress Series*, *398*, 259-274.

Rayshubskiy, A., Holtz, S. L., D'Alessandro, I., Li, A. A., Vanderbeck, Q. X., Haber, I. S., ... & Wilson, R. I. (2020). Neural circuit mechanisms for steering control in walking Drosophila. *BioRxiv*, 2020.04.04.024703. https://doi.org/10.1101/2020.04.04.024703

Ros, I. G., Omoto, J. J., & Dickinson, M. H. (2024). Descending control and regulation of spontaneous flight turns in Drosophila. *Current Biology*, *34*(3), 531-540.

Sapkal, N., Mancini, N., Kumar, D. S., Spiller, N., Murakami, K., Vitelli, G., ... & Bidaye, S. S. (2023). Neural circuit mechanisms underlying context-specific halting in Drosophila. *bioRxiv*, 2023.09.25.559438. https://doi.org/10.1101/2023.09.25.559438

Scheffer, L. K., Xu, C. S., Januszewski, M., Lu, Z., Takemura, S. Y., Hayworth, K. J., Huang, G. B., Shinomiya, K., Maitlin-Shepard, J., Berg, S., Clements, J., Hubbard, P. M., Katz, W. T., Umayam, L., Zhao, T., Ackerman, D., Blakely, T., Bogovic, J., Dolafi, T., Kainmueller, D., … Plaza, S. M. (2020). A connectome and analysis of the adult *Drosophila* central brain. *eLife*, *9*, e57443. https://doi.org/10.7554/eLife.57443

Shik, M. L., Severin, F. V., & Orlovskiĭ, G. N. (1966). Upravlenie khod'boĭ i begom posredstvom elektricheskoĭ stimulatsii srednego mozga [Control of walking and running by means of electric stimulation of the midbrain]. *Biofizika*, *11*(4), 659–666.

Shtonda, B. B., & Avery, L. (2006). Dietary choice behavior in Caenorhabditis elegans. *The Journal of experimental biology*, *209*(Pt 1), 89–102. https://doi.org/10.1242/jeb.01955

Sirota, M. G., Di Prisco, G. V., & Dubuc, R. (2000). Stimulation of the mesencephalic locomotor region elicits controlled swimming in semi-intact lampreys. *The European journal of neuroscience*, *12*(11), 4081–4092. https://doi.org/10.1046/j.1460-9568.2000.00301.x

Sommerfeld, J., Kato, A., Ropert-Coudert, Y., Garthe, S., & Hindell, M. A. (2013). Foraging parameters influencing the detection and interpretation of area-restricted search behaviour in marine predators: a case study with the masked booby. *PloS one*, *8*(5), e63742. https://doi.org/10.1371/journal.pone.0063742

Staudacher, E. (1998). Distribution and morphology of descending brain neurons in the cricket Gryllus bimaculatus. *Cell and Tissue Research*, *294*, 187-202.

Steck, K., Veit, D., Grandy, R., Badia, S. B., Badia, S. B., Mathews, Z., Verschure, P., Hansson, B. S., & Knaden, M. (2012). A high-throughput behavioral paradigm for Drosophila olfaction - The Flywalk. *Scientific reports*, *2*, 361. https://doi.org/10.1038/srep00361

Steeves, J. D., Sholomenko, G. N., & Webster, D. M. (1987). Stimulation of the pontomedullary reticular formation initiates locomotion in decerebrate birds. *Brain research*, *401*(2), 205-212.

Steinbeck, F., Nowotny, T., Philippides, A., & Graham, P. (2022). Production of adaptive movement patterns via an insect inspired spiking neural network central pattern generator. *Frontiers in Computational Neuroscience*, *16*, 948973.

Stone, T., Webb, B., Adden, A., Weddig, N. B., Honkanen, A., Templin, R., ... & Heinze, S. (2017). An anatomically constrained model for path integration in the bee brain. *Current Biology*, *27*(20), 3069-3085.

Stupski, S. D., & van Breugel, F. (2023). Wind Gates Search States in Free Flight. *bioRxiv* 2023.11.30.569086. https://doi.org/10.1101/2023.11.30.569086

Tao, L., Ozarkar, S., Beck, J. M., & Bhandawat, V. (2019). Statistical structure of locomotion and its modulation by odors. *eLife*, *8*, e41235. https://doi.org/10.7554/eLife.41235

Tao, L., Ozarkar, S., & Bhandawat, V. (2020). Mechanisms underlying attraction to odors in walking Drosophila. *PLoS computational biology*, *16*(3), e1007718. https://doi.org/10.1371/journal.pcbi.1007718

Tastekin, I., Riedl, J., Schilling-Kurz, V., Gomez-Marin, A., Truman, J. W., & Louis, M. (2015). Role of the subesophageal zone in sensorimotor control of orientation in Drosophila larva. *Current Biology : CB*, *25*(11), 1448–1460. https://doi.org/10.1016/j.cub.2015.04.016

van Breugel, F., & Dickinson, M. H. (2014). Plume-tracking behavior of flying Drosophila emerges from a set of distinct sensory-motor reflexes. *Current Biology : CB*, *24*(3), 274–286. https://doi.org/10.1016/j.cub.2013.12.023

Westeinde, E. A., Kellogg, E., Dawson, P. M., Lu, J., Hamburg, L., Midler, B., Druckmann, S., & Wilson, R. I. (2024). Transforming a head direction signal into a goal-oriented steering command. *Nature*, 10.1038/s41586-024-07039-2. Advance online publication. https://doi.org/10.1038/s41586-024-07039-2

Yang, H. H., Brezovec, L. E., Capdevila, L. S., Vanderbeck, Q. X., Adachi, A., Mann, R. S., & Wilson, R. I. (2023). Fine-grained descending control of steering in walking *Drosophila*. *bioRxiv* 2023.10.15.562426. https://doi.org/10.1101/2023.10.15.562426

York, R. A., Brezovec, L. E., Coughlan, J., Herbst, S., Krieger, A., Lee, S. Y., Pratt, B., Smart, A. D., Song, E., Suvorov, A., Matute, D. R., Tuthill, J. C., & Clandinin, T. R. (2022). The evolutionary trajectory of drosophilid walking. *Current Biology : CB*, *32*(14), 3005–3015.e6. https://doi.org/10.1016/j.cub.2022.05.039